Additive Manufacturing 84 (2024) 104144

Contents lists available at ScienceDirect

Additive Manufacturing

journal homepage: www.elsevier.com/locate/addma

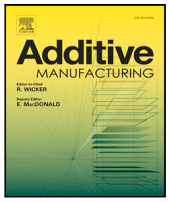

Research paper

A methodology for the 3D characterization of surfaces using X-ray computed tomography: Application to additively manufactured parts

Florian Steinhilber [a,*], Joel Lachambre [a], David Coeurjolly [b], Jean-Yves Buffiere [a], Guilhem Martin [c], Remy Dendievel [c]

[a] INSA Lyon, CNRS, MATEIS, Villeurbanne, F-69621, France
[b] Université de Lyon, CNRS, INSA Lyon, UCBL, LIRIS, Villeurbanne, F-69621, France
[c] Université Grenoble Alpes, CNRS, Grenoble INP, SIMAP, Grenoble, F-38000, France

ARTICLE INFO

Keywords:
3D surface characterization
X-ray computed tomography
Roughness
Curvature
Additive manufacturing

ABSTRACT

Many studies highlight the significance of three-dimensional surface topography characterization in assessing its effect on the mechanical or functional properties of materials. This is especially obvious for parts made by additive manufacturing (AM), known for their complex shape and surface topographies. However, a vast majority of 3D characterizations have constraints regarding the macroscopic geometry of the parts they can probe. At the microscale, they are also unable to account for hidden surface features, e.g. notches hidden by unmelted powder particles. Even with the use of X-ray Computed Tomography (XCT) — a tool with the potential to circumvent these issues — data is often reduced to 2D or 2.5D formats for easier analysis, but this leads to a loss of information. This underscores the need for XCT data post-treatment tools to perform thorough 3D surface characterizations. Herein, we introduce a methodology for local roughness and curvature characterization of surfaces of complex shapes using XCT. This method has been designed to be user-friendly, especially for those without extensive data analysis expertise. It provides a comprehensive 3D characterization and efficiently tackles the issues caused by hidden features. After a detailed description of our methodology, we give a first illustrative example based on architected structures fabricated by Electron Powder Bed Fusion (E-PBF). By integrating roughness and curvature metrics, we also derive a parameter indicative of the stress concentrations caused by surface irregularities.

1. Introduction

Surface topography has a large influence on many functional and mechanical properties of materials. In biomedical applications, implants surface roughness is for instance suspected to have an impact on osseointegration [1,2] and has been shown to foster bacteria adhesion [3,4]. For load-bearing structures, surface topography alone may lead to premature failure if poorly controlled [5,6]. For example, a rough surface typically has a large area of contact with its environment, possibly accelerating corrosion mechanisms [7]. The presence of surface defects also creates stress concentrations that can lead to crack initiations and thus result in poor fatigue properties [8]. Rough as-built surfaces inherited from additive manufacturing are also more prone to hydrogen embrittlement than polished ones [9]. All these examples emphasize the need for a detailed characterization of surface topography.

In parallel, advancements in material processes are leading to increasingly intricate surfaces. This is particularly the case in Additive Manufacturing (AM), which is gaining considerable attention. Since AM allows greater design freedom, additively manufactured parts often show more complex shapes than those obtained with conventional processes. Architected structures are a typical example [10,11]. In such cases, standard contact-based roughness instruments or optical systems provide incomplete information due to limited access to the surface. Additionally, at the micro-scale, surfaces inherited from AM exhibit a large variety of *surface features*, such as notches, unmelted powders, or dross [8,12,13]. The interaction between all those surface features can make surface analysis even more challenging. For instance, overhanging surface features or unmelted powder particles can hide underlying notches, as depicted in Fig. 1. This complexity highlights the need for both instruments and analysis tools that can accurately characterize complex 3D structures and surface features.

While many studies report 3D roughness analyses, stricto sensu most of them are not fully 3D measurements. These approaches have limitations in terms of sample geometry and surface features they

* Corresponding author.
E-mail address: florian.steinhilber@insa-lyon.fr (F. Steinhilber).

https://doi.org/10.1016/j.addma.2024.104144
Received 17 November 2023; Received in revised form 24 March 2024; Accepted 11 April 2024
Available online 14 April 2024

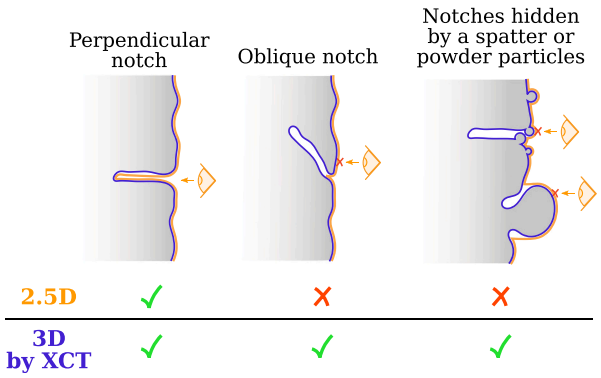

Fig. 1. Schematic showing the interest of characterizing AM as-built surfaces in 3D using XCT. Several examples are shown, corresponding to different surface defects. The orange lines show surfaces as seen by a 2.5D characterization tool which probes the surface from a single point of view and without the ability to look through matter. The blue lines correspond to the true surfaces, i.e. the ones that would ideally be obtained through XCT using a high resolution, with no noise nor artifacts. In two of the three examples shown, the 2.5D surface characterization fails to account for notches because they are hidden by other surface features. (For interpretation of the references to color in this figure legend, the reader is referred to the web version of this article.)

can characterize. These limitations can originate from the instruments used for raw surface acquisition, such as interferometers or confocal microscopes. The data representation used for subsequent analysis can also lead to information loss. To clarify this, key concepts will be introduced hereafter to differentiate existing approaches for 3D surface characterization and their actual ability to characterize complex 3D structures and surface features.

Surface characterization often involves optical instruments like white light interferometers or confocal microscopes [14–18]. These instruments use *unidirectional* light sources, characterizing the surface from a single perspective. Consequently, surface topography is projected onto a single plane — the one perpendicular to the light source. This yields height maps with a single z-coordinate value for each (x,y) point on a regular grid. As the third (z-axis) dimension is only partially used, this data representation can be referred to as *2.5D* [19,20]. Accordingly, instruments like interferometers or confocal microscopes will be termed 2.5D instruments hereafter.

2.5D characterization is feasible for surfaces with simple geometries like planes or cylinders. For complex surfaces, irregularities often prevent the measurement tool from accessing some areas. This is obvious in AM parts with sophisticated geometries. Even when aiming at characterizing flat and accessible regions, limitations persist if the surface topography includes hidden features. This effect is depicted in Fig. 1. Orange lines in Fig. 1 show that a 2.5D surface characterization manages to describe a notch only if the latter is perpendicular to the surface. It fails if the notch is oblique or hidden by partially melted powders and/or spatters.

In order to overcome such limitations, developments have recently been made in the field of *free-form metrology* [21,22], which aims at characterizing surfaces of complex and arbitrary shapes. Raw surface acquisition can now be achieved through instruments like structured light scanners [23,24] or commercial X-ray tomographs [16,20,25–27]. These tools offer *omnidirectional* characterization, thereby facilitating the characterization of complex surfaces. To fully harness this omnidirectional capability, alternative data representations are required. The 2.5D representation limits each (x,y) point to only one z-coordinate, imposing a substantial constraint. To mitigate this, free-form metrology adopts surfaces represented as meshes or point clouds composed of three-dimensional points (x,y,z). Multiple points with identical x and y coordinates can thus exist.

While the free-form surface representation is versatile, it requires novel analysis techniques different from 2.5D methodologies, e.g. for surface filtering. Although some studies have employed free-form representations [22,26,28,29], this approach is rarely used. Even when surfaces are captured using methods like XCT, they are often reduced to 2.5D height maps for subsequent analysis [16,20,30–32]. This trend stems from the fact that surface analysis operations, such as filtering or roughness parameters measurement, can be much more complicated when using a complete 3D representation instead of a simpler 2.5D one [21].

Thus, some technical issues still need to be overcome to obtain more robust results. Even when the existing solutions may be sufficient, they are often sophisticated and therefore not necessarily user-friendly. They require advanced computer programming skills to be implemented and important computational resources. Further work is thus needed to address these challenges and promote the broader adoption of free-form metrology.

Another distinction can be made between instruments that are able to look through matter (e.g. XCT) and those that are not (e.g. structured light scanning). Although 3D light scanning enables the characterization of complex geometries, it will actually be limited for parts with inaccessible areas (e.g. lattice structures or internal channels) or too complex/small surface features. On the contrary, the ability of XCT to look through matter and have access to internal features enables — at least in theory — the characterization of any shape as well as hidden surface features. Hence, as depicted by blue lines in Fig. 1, XCT succeeds in properly accounting for complex 3D surface features such as notches hidden by unmelted powder, provided that the spatial resolution is sufficiently high.

Note that for now, the spatial resolution accessible for each instrument has not been discussed yet. Typically, 2.5D tools achieve superior resolutions compared to XCT, even though recent progress in XCT has made micron-level resolutions feasible using laboratory sources.

Table 1 summarizes the different factors that can influence the ability of the various instruments to properly characterize surfaces with intricate 3D macroscopic shapes and/or hidden microscopic surface features.

Beyond the question of performing a true 3D surface characterization, it may be important to question which information is the most relevant to extract from it. Most often, roughness characterization is reduced to the analysis of a few roughness parameters that characterize the height distribution of the surface. However, depending on the aim of the study, the surface height distribution may not contain all relevant information. For instance, the stress concentration caused by surface notches is known to be dependent not only on the notch depth (quantified by parameters such as the maximum notch depth S_v) but also on the curvature at its root [33].

Table 1
Factors influencing the ability of different instruments to properly characterize surface with complex macroscopic shapes and hidden surface micro-features (e.g. notches hidden by unmelted powder particles).

	2.5D instruments	Structured light scanning	XCT
Source directionality	Unidirectional	Omnidirectional	Omnidirectional
Data representation	2.5D	3D possible	3D possible
Ability to look through matter	No	No	Yes
Ability to characterize complex 3D components	No	Yes	Yes
Ability to account for hidden micro-features	No	No	Yes

Hence, various models exist that attempt to predict fatigue life by combining roughness and curvature measurements. Examples include the models of Neuber [34], Arola and Ramulu [35], and Lee et al. [36]. Although these models show some conclusive results, they were also found to produce inaccurate estimations in some cases [37,38]. It is worth noting that they have mostly been applied to regular machined surfaces [38–41]. Although some recent studies have attempted to extend it to as-built surfaces inherited from AM [36,42], this area requires further exploration.

From a more technical point of view, some improvements could be made to enhance curvature measurements and the resulting mechanical prediction accuracy. Many of the studies performed them from 2.5D [41,43] or 2D [36–40,42] data. Such an approach might significantly bias curvature values, similar to the issues observed with roughness measurements. Moreover, when calculating curvature in 2.5D or 3D, various definitions can be considered, e.g. principal, Gaussian, and mean curvature. The choice among these can significantly affect the results. Consequently, it is crucial to select a relevant one based on the intended application. As for now, there is a lack of clear guidance for choosing one definition over another. These issues are an additional motivation for this study.

This study introduces a workflow for 3D surface characterization using XCT, measuring both roughness and curvature. By combining these two measurements, we propose a parameter representative of the severity of surface features with respect to mechanical properties. The aim is also to demonstrate the benefit of characterizing surfaces inherited from AM as free-form surfaces, taking into account hidden micro-features and opening new avenues to characterize components showing intricate macroscopic shapes. This approach was designed to be applied to AM samples, but it could also be employed in a broader context, e.g. for as-cast surfaces. An effort was made to ensure its accessibility, i.e. without the need for advanced programming and image analysis skills.

For more details about the presented methodology and its application, the reader is redirected to the PhD thesis of Steinhilber [44]. In particular, the methodology is used to study the influence of surface roughness on fatigue properties of Ti64 samples produced by Electron beam Powder Bed Fusion (E-PBF) and Laser Powder Bed Fusion (L-PBF).

2. Materials and XCT data acquisition

Different samples were used to demonstrate the application of the developed workflow. All were manufactured by Electron Powder Bed Fusion (E-PBF) using an ARCAM A1 machine and Ti64 powders. To characterize their as-built surface, no surface treatment was applied. Powder grain size distribution ranged from 60 µm to 100 µm and the layer thickness was set to 50 µm. More details about the processing conditions can be found in Persenot et al. [8]. To characterize their surface, samples were scanned using laboratory XCT.

A 2 mm vertically built cylinder was first used as a simple example. It was scanned using a cone beam Phoenix V|tome|x laboratory tomograph with a voltage of 90 kV, a current of 240 µA, an exposure time of 333 ms and 720 projections. No physical filter was used during the scan acquisition, but a numerical filter was used for beam hardening correction. Reconstruction was performed using a standard filtered back projection algorithm (phoenix datos *x* software). The voxel size used was 2.5 µm, but volumes were downscaled by a factor 2 before further analysis.[1] The resulting voxel size is therefore 5 µm.

Two as-built Ti64 architected structures were also characterized: a gyroid structure [11,46,47] and an octet-truss lattice structure, see Fig. 2.

[1] The data were retrieved from the work of Persenot [45], who performed this downscaling to reduce data size.

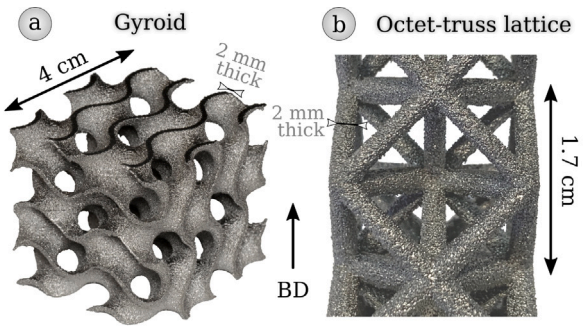

Fig. 2. Ti64 architected structures fabricated by E-PBF. (a) Gyroid structure. (b) Octet-truss lattice structure.

XCT scans were made with an RX Solutions laboratory tomograph using a Cu filter to mitigate beam hardening artifacts. The main acquisition parameters are summarized in Table 2. Two scans were acquired at different resolutions for the gyroid structure. For all architected structures, reconstructions were done using an implementation of FDK algorithm [48].

Table 2
Acquisition parameters for XCT scans performed using the RX Solutions tomograph.

	Gyroid (5 µm)	Gyroid (10 µm)	Octet truss
Voxel size (µm)	5	10	10
V (kV)	230	230	230
I (µA)	35	70	58
Cu filter (mm)	1.4	1	1
Number of projections	3616	3616	2240
Exposure time (ms)	2000	333	500

All XCT scans were converted to 8-bit after reconstruction to reduce data size. After conversion, volumes size were 158 MB, 4.6 GB and 5.1 GB for the cylinder, the gyroid (10 µm scan) and the octet-truss lattice respectively.

3. 3D surface characterization methodology

3.1. Surface extraction

The first step of surface characterization is its extraction from the XCT scan. Since it can be affected by noise, a noise-reducing filter is applied to the reconstructed volume before further calculations. An edge-preserving filter is used to preserve a detailed description of the surface [49]. A volumetric median filter is used as it provides satisfying results while keeping computing time reasonable for large volumes.

After filtering, the sample is segmented through thresholding of the volume's histogram. Other techniques such as local iterative fitting [25] or gradient-based methods [50] could also be interesting alternatives worth investigating in future studies. Here, with thresholding we aim at separating the two main peaks of the grayscale histogram, which will be referred to as dark (voids) and bright (sample) peaks — see Fig. 3a. Several methods can be used to automatically determine an optimal threshold. One of the most popular is Otsu's method [51,52]. The latter makes the assumption that all voxels are separated into two classes based on their gray level while minimizing the inter-class variance. It yields in most cases consistent and robust results.

However, it may not always be the best choice if one is looking for some specific surface features such as surface defects that will be prone to initiate failure during mechanical loading. In this specific case, partially melted particles are unlikely to be of much interest. They can even hide more severe surface defects such as notches. Contrariwise, deep and sharp notches are very often the most critical defects and

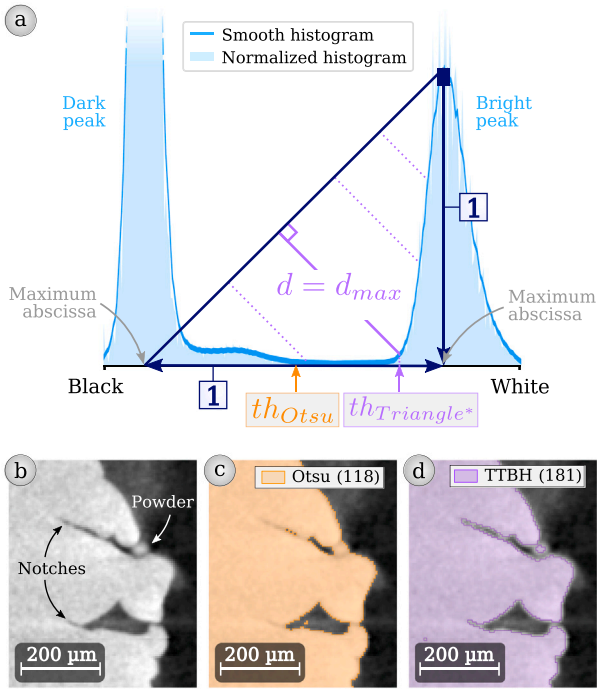

Fig. 3. (a) Definition of the TTBH, illustrated based on the E-PBF cylinder normalized grayscale histogram. (b) XCT 8-bit radial slice showing two sharp notches and a partially melted powder (voxel size = 5 µm). (c) Otsu's threshold application (orange area) (d) TTBH application (purple area). (For interpretation of the references to color in this figure legend, the reader is referred to the web version of this article.)

are therefore of great interest. However, the sharpest ones are often difficult to segment from XCT data, because the corresponding voxels show intermediate grayscale values. This leads Otsu's method to consider many of them as foreground voxels, erasing notches from the surface although they are the most interesting defects when questions related to crack initiation and failure must be tackled.

This effect can be seen in Figs. 3b and 3c. Fig. 3b shows an XCT radial slice of a 2 mm as-built E-PBF cylinder, where two deep notches can be seen. Fig. 3c shows in orange the pixels considered as foreground using Otsu's threshold for surface extraction. It can be seen that both notches are not properly accounted for when using Otsu's threshold, although they are clearly visible on the grayscale image in Fig. 3b.

A threshold corresponding to a higher grayscale value than Otsu's one will be certainly more adapted to capture such severe surface defects. Indeed, both partially melted particles and sharp notches typically show intermediate grayscale values because they are at the interface between matter and air. Thus, selecting a threshold that stands at the end of the plateau — just at the left border of the histogram's bright peak — will enable to discard some parts of unmelted powder particles while better capturing sharp notches.

The thresholding method proposed is inspired by the triangle threshold introduced by Zack et al. [53]. It is thereafter referred to as the *Triangle Threshold for Bimodal Histograms (TTBH)*. Its principle is described schematically in Fig. 3a.

First, if the histogram is too noisy, it may be useful to smooth it. In the present work, a moving average of size 10 is applied. Second, the histogram is normalized so that both the bright peak maximum and the distance between the two histogram peaks are equal to 1. Finally, the desired threshold is simply the gray value which maximizes the distance d as defined in Fig. 3a. As required, the obtained threshold is located just at the left edge of the bright peak. Fig. 3d shows that the two sharp notches are clearly better captured using the TTBH than by Otsu's method. The powder grain is cropped, which can be both an advantage and a drawback, depending on which surface features one aims to characterize.

It may be worth mentioning that this thresholding method is particularly sensitive to noise and artifacts (e.g. beam hardening). This can be at least partially compensated by the use of the proper noise-reducing filter beforehand. It may also be relevant in some cases to make a compromise between the TTBH and Otsu's threshold. A simple and convenient way to do that can be to calculate both and take an intermediate value.

Following thresholding, the volume undergoes a cleaning process to remove all internal pores or tiny objects caused by measurement noise.[2] This cleaned binary volume is subsequently referred to as the *sample mask*, illustrated in Fig. 4b. In our case, the sample surface is defined as the *surface mask* depicted in Fig. 4c. It is the binary mask whose foreground is composed of all surface voxels. These surface voxels are the foreground voxels of the sample mask which have at least one background voxel as first neighbor. A connectivity of 1 is used to determine neighbors.

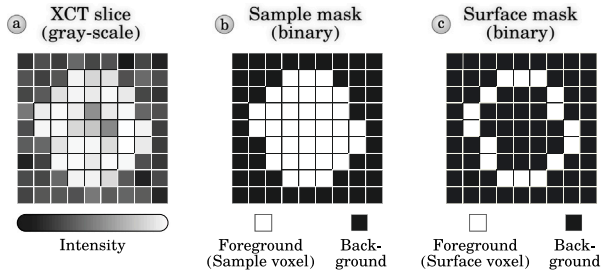

Fig. 4. (a) Schematic example of a grayscale XCT slice. (b) Corresponding sample mask. (c) Corresponding surface mask.

3.2. 3D roughness calculation

The topography of a surface is often divided into 4 components, each one corresponding as a first approximation to a range of spatial frequencies: the object's form, the waviness, the roughness, and the micro-roughness [54,55]. Most commonly, only the roughness component is considered significant for characterizing surface micro-features such as notches or unmelted powder particles. The form and waviness typically represent geometric deviations, while micro-roughness is often viewed as measurement noise. The objective is therefore to discriminate roughness from these other components to achieve a complete surface characterization.

In the case of a conventional 2.5D surface characterization, the shape of the characterized surface is necessarily simple (plane, cylinder...). Form removal, which consists of subtracting the component geometry, can thus be done rather easily using least-squares optimization. Filters are then used to discriminate roughness from waviness (L-filter) and micro-roughness (S-filter). In both cases, the Gaussian filter is the default option [55].

However, 2.5D characterization is only possible for parts with simple geometries, as discussed in Section 1. In order to take full advantage of XCT, a 3D surface representation must be used — e.g. a mesh or a point cloud made of points with arbitrary (x,y,z) coordinates. In this case, the roughness characterization workflow can be more challenging. In particular, the form removal step is complex when no analytical

[2] The volume is cleaned from small objects by labeling the binarized volume and keeping only the largest object (= the volume of interest). Pores are then removed by inverting the obtained volume (logical NOT operation), keeping the largest object (= the background) using labeling, and inverting the volume again.

expression is adapted. For 3D printed parts, a first approach consists of using the CAD file as a reference. This is sometimes done to measure geometrical deviations between the manufactured part and its CAD model [30,56–58]. However, this requires the geometrical deviations to be small enough to get an accurate measurement.

If the CAD file cannot be used, it is possible to smooth the raw surface and use the result as a reference. In this case, the roughness is defined as the distance between the surface and a smoothed version of it. A number of studies already addressed this topic, see the work of Jiang and Scott [21] for an extensive review. In such studies, surfaces are generally meshed and may be smoothed using morphological filters [26,59], diffusion-based filters [60], anisotropic diffusion-based filters [61], or wavelet decomposition [62].

The methodology presented here follows the same principle of surface smoothing and distance measurement. It can thus be applied to complex geometries without any need for a prior knowledge. However, unlike most common processing workflows, in our case, the surface is not extracted as a mesh for calculations. Instead, all calculations are done on the digital volume obtained by XCT. One of the advantages is that it can be implemented in standard open-source image analysis software such as ImageJ. The overall image analysis workflow is schematically illustrated in Fig. 5. Two implementations using either ImageJ or Python can also be accessed via an online repository [63].

The proposed workflow only uses as input data the sample mask, whose computation is detailed in Section 3.1.

The first step is the computation of the surface mask — also defined in Section 3.1. The latter will be used at the end of the workflow to extract data from volumes only at the voxels of interest — i.e. the surface voxels. The surface mask can be obtained by applying an erosion to the sample mask, and then computing the logical XOR operation between the sample mask and the result of the erosion.

The second step of the workflow is the smoothing step. It is done here by converting the sample mask to float or integer values and applying a 3D Gaussian filter.[3] The chosen degree of smoothing will determine the limit between roughness on the one hand and waviness/form

[3] An alternative solution, not developed here, would be to perform smoothing by applying a 3D morphological filter [21,64] on the sample mask.

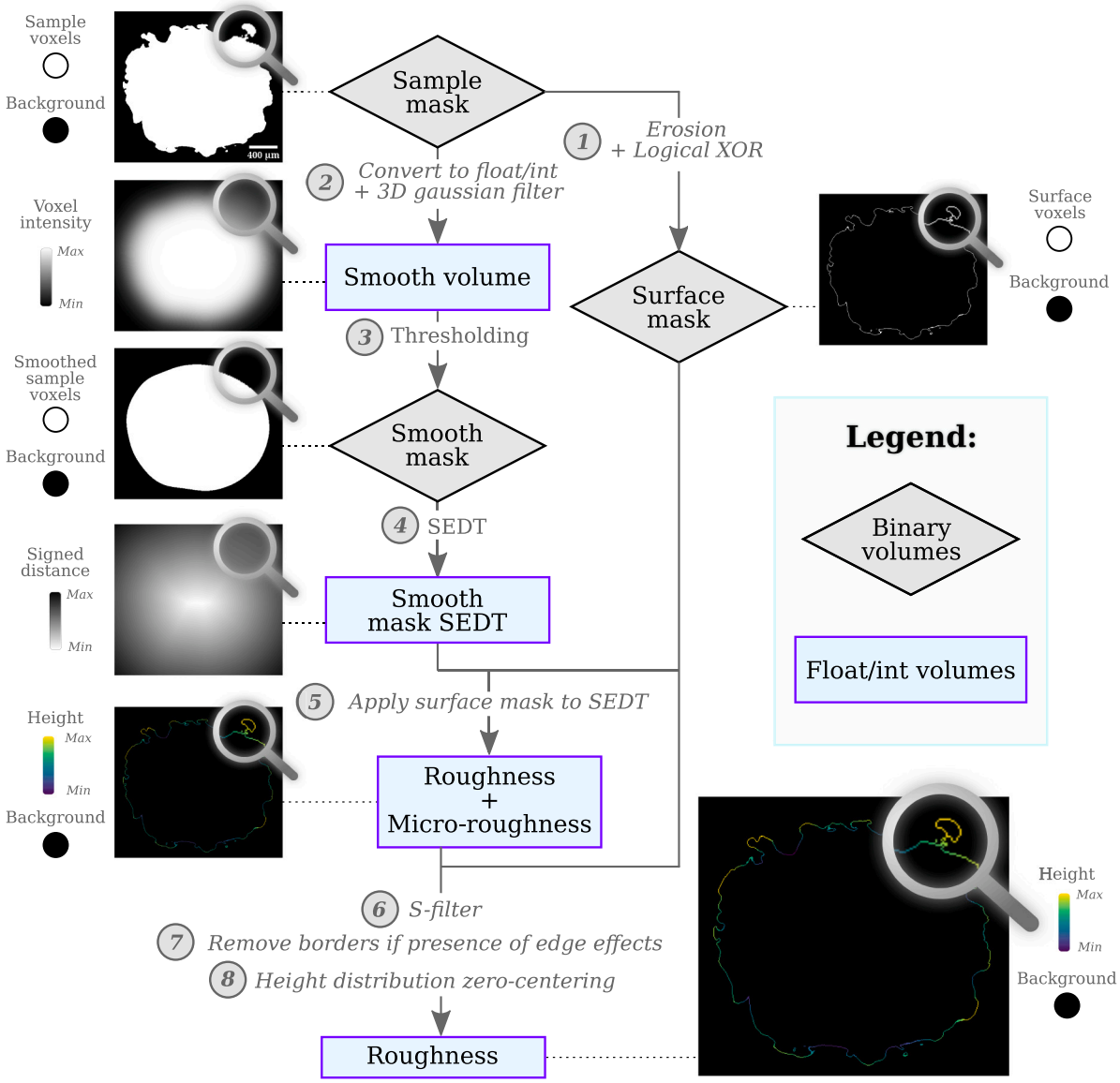

Fig. 5. Workflow proposed for the 3D roughness computation. The sample mask and surface mask are defined in Fig. 4. The images shown correspond to transverse cross-sections of a 2 mm E-PBF Ti64 cylinder at different steps of the calculation.

on the other hand. It is quantified by the *cut-off wavelength* λ_c [65], which is the wavelength considered to discriminate form and waviness from roughness. From an image processing point of view, a Gaussian filter is more often adjusted using the standard deviation σ, which can be easily derived from the cut-off wavelength λ_c following Eq. (1).

$$\sigma = \sqrt{\frac{\ln 2}{2}} \cdot \frac{\lambda_c}{\pi} \approx 0.187 \cdot \lambda_c \tag{1}$$

ISO standards provide rules to appropriately set the value of the parameter λ_c [55]. Although they are meant for 2D filters applied to height maps, they are used by extension in the developed workflow to adjust the 3D Gaussian filter. Ideally, the choice should be made by observing the surface and identifying the features that need to be characterized as roughness. It is then advised to set λ_c to be five times the size of the largest feature of interest, choosing among a list of predetermined values (0.25 mm, 0.8 mm, 2.5 mm, etc.) [55]. This choice is somewhat arbitrary, and is highly dependent on the surface state inherited from the AM process used, as well as on the specific surface features one seeks to characterize. This can explain the wide variations in values used in the literature on AM materials, and the fact that they can differ significantly from the values used for smoother surfaces inherited from conventional processes [66]. Grazia Guerra and Lavecchia [28] used for example a cut-off wavelength of 0.25 mm while Vetterli et al. [67] used several values up to 2 mm.

In the third step of the workflow, the smoothed volume obtained after filtering is segmented by thresholding. This results in a smoothed version of the sample mask, hereafter referred to as the smooth mask. The latter is then used as reference for roughness calculation. The most straightforward choice for the threshold value is the mean of background and foreground voxels values (e.g. 127.5, if the background is 0 and foreground voxels are 255). However, this leads in general to some volume shrinkage, especially for large λ_c values. To avoid this problem, the threshold value is instead determined automatically so that the smooth mask volume equals the volume of the original mask. The obtained threshold is, for instance, 118 in the case shown in Fig. 5 ($\lambda_c = 0.8$ mm).

The fourth step aims at computing the distance between the sample surface and its smoothed version. For this purpose, the Signed Euclidean Distance Transform (SEDT) [69,70] is computed from the smooth mask. This results in a float volume where the value at each foreground voxel is the distance to the nearest background voxel, and contrariwise for the values at the background voxels. The distances are signed, e.g. positive for background voxels and negative for foreground voxels.

At the fifth step, the surface mask is applied to the smooth mask SEDT. This results in a sparse volume where most of the voxels have the same background value (e.g. 0), except the surface voxels which hold the distances to the smooth mask, i.e. the sought roughness values.

The sixth step consists in applying an S-filter. This aims at removing the highest frequencies, in other words, the micro-roughness. The standard filter used for this purpose is again a Gaussian filter [55]. The cut-off wavelength used for this filter is commonly denoted λ_S. A procedure to calculate the S-filter using 3D Gaussian filters only based on normalized convolution [71] is described in Appendix. This filtering step becomes particularly relevant if the voxel size set for XCT scans is not small enough to properly describe the surface topography. When the voxel size approaches the dimensions of surface features, the surface tends to be oversimplified and discretized, yielding a staircase appearance. Such oversimplification can result in sharp fluctuations in the roughness measurement. Using the S-filter helps to moderate those abrupt changes.

The seventh step addresses edge effects that arise due to Gaussian filtering [72]. When computing the filtered value for a particular voxel using the Gaussian kernel, surrounding voxels are taken into account. However, for those voxels near the XCT scan boundary, the convolution radius might extend past this boundary. For these voxels, the XCT scan has to be extrapolated, for instance using an arbitrary constant value. The most common choice is 0. This value aligns well with our needs since 0 represents the background value that is assumed to envelop the sample. However, this method can result in biased values for surface voxels too close to the scan boundary. For example, in the context of a cylinder scan, the topmost and bottommost surface voxels may contain such biased values.

Various solutions have been suggested to address this challenge for 2D or 2.5D roughness measurements [73]. The most straightforward one is to discard roughness values for points located too close to the edges, typically within a distance of the cut-off value or half of it. In the described workflow, the approach adopted involves cropping the upper and lower borders by a width of $\frac{\lambda_c}{2}$ wherever necessary. However, if this method results in discarding too much data, other strategies, based

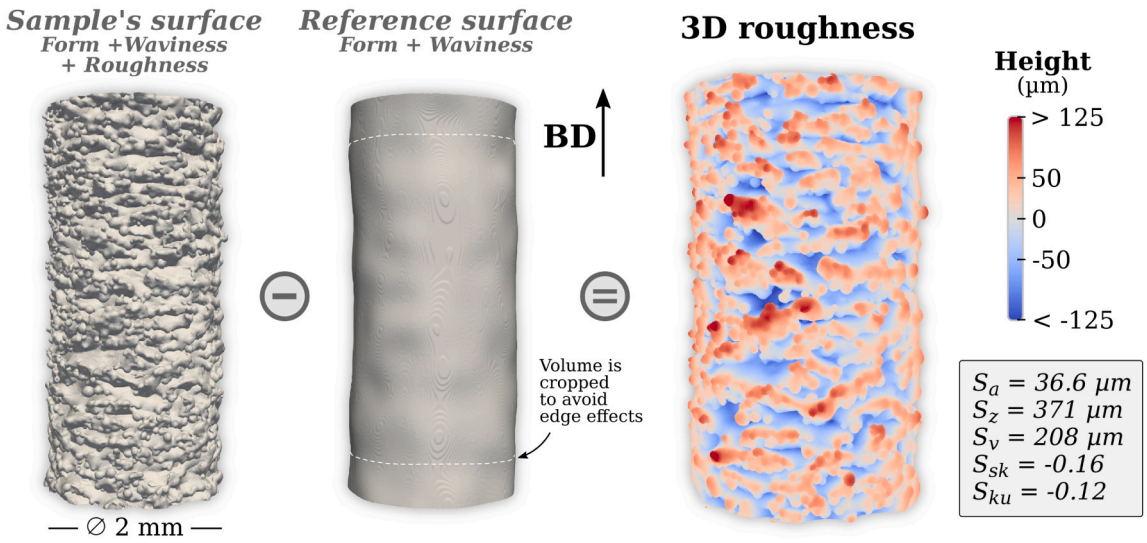

Fig. 6. Surface roughness measurements, as described in Fig. 5, applied to a 2 mm diameter as-built E-PBF cylinder. Computations were made from an XCT scan with a voxel size of 5 µm. Cut-off values were set to $\lambda_c = 0.8$ mm and $\lambda_S = 0.015$ mm. To avoid edge effects, points closer to the boundaries than $\frac{\lambda_c}{2}$ were discarded. Formulas for roughness parameters computation are given in the ImageJ and Python scripts in an online repository [63]. For more insights on the methods that can be used to measure roughness parameters on free-form surfaces, the interested reader is invited to look at [68].

on extrapolation or the use of normalized convolution [71], can be employed in the Gaussian filtering step. This would allow the user to address edge effects without the need to truncate volumes later on.

Lastly, the eighth step ensures that the height distribution is zero-centered, meaning the average height is zero. This condition is intuitive and is assumed when computing some roughness parameters such as S_{sk} and S_{ku}. To achieve this, the average height is subtracted from the height of each surface voxel.

An example of roughness calculated on a 2 mm diameter cylinder fabricated by E-PBF is shown in Fig. 6. The initial sample's surface and the smooth reference one are displayed, as well as the derived roughness. For improved visualization, surfaces represented solely as raw geometry, without additional data such as roughness, were meshed using the marching cubes algorithm. The mesh representation enables to display shading, making volume perception possible. This method was applied to the two left-sided cylinders shown in Fig. 6, as well as further on in Fig. 9a-b. In all other cases, surfaces are displayed as point clouds made of the surface voxels used for computations. Each point is depicted as a uniform circular disk (no shading), with its color determined by the scalar value measured at that particular point, such as roughness. Despite the dense distribution of points potentially suggesting a smooth surface, closer inspection would reveal the discrete nature of the surface, a characteristic most visible in Fig. 9c-e.

The triangle threshold for bimodal histograms presented in Section 3.1 was used for surface extraction and a cut-off wavelength λ_c of 0.8 mm has been chosen for roughness calculation. Regarding the S-filter cut-off λ_s, a value of three times the voxel size (0.015 mm) was used. Note that points closer than $\frac{\lambda_c}{2}$ to the upper and lower boundaries were discarded at the end of the computation.

As far as computational performance is concerned, the use of 3D operations makes the presented methodology demanding in terms of Random Access Memory (RAM). This can be a limitation for large volumes, which can be overcome to a certain extent by dividing the volume and performing computations in several steps. Processing time is nonetheless reasonably low since efficient implementations exist for the operations used. As an example, the computation for the 158 MB XCT scan of the cylinder in Fig. 6 took around 1 min on a conventional laptop with 8 CPU cores and using the ImageJ macro that can be accessed via the online repository [63]. A Python implementation is also given in Steinhilber [63], with some improvements to limit RAM usage and significantly increase computation speed.

3.3. 3D curvature calculation

The curvature κ is a measure of how a curve (in 2D) or a surface (in 3D) bends at a particular point. For a curve, it corresponds to the inverse of the radius ρ of the osculating circle at this given point, as schematically shown in Fig. 7a.

Curvature is a more complex concept for surfaces and several definitions exist. The closest 3D equivalent of the curvature in 2D would be the *directional curvature*, which measures how much the surface bends along a particular direction. It is positive when the surface bends outwards, and negative otherwise. Two directions are of particular interest: the direction of *minimum curvature* $\vec{d}_{min}$ and the one of *maximum curvature* $\vec{d}_{max}$, also known as *principal directions*. The corresponding curvatures are the principal curvatures κ_{min} and κ_{max}, see Fig. 7b.

Knowing principal directions and curvatures, the directional curvature in any direction can be derived using Eq. (2) [74]. Finally, it is also common to use the average of both principal curvatures, the mean curvature κ_{mean}, or their product, the Gaussian curvature κ_{gauss}.

$$\kappa\left(\vec{v}\right) = \begin{pmatrix} v_n \\ v_{min} \\ v_{max} \end{pmatrix}^{\mathsf{T}} \cdot \begin{pmatrix} 0 & 0 & 0 \\ 0 & \kappa_{min} & 0 \\ 0 & 0 & \kappa_{max} \end{pmatrix} \cdot \begin{pmatrix} v_n \\ v_{min} \\ v_{max} \end{pmatrix} = v_{min}^2 \cdot \kappa_{min} + v_{max}^2 \cdot \kappa_{max} \quad (2)$$

where $\kappa\left(\vec{v}\right)$ is the directional curvature in the direction $\vec{v}$, $\vec{v} = v_n \cdot \vec{n} + v_{min} \cdot \vec{d}_{min} + v_{max} \cdot \vec{d}_{max}$ is an arbitrary vector and $\vec{n} = \vec{d}_{min} \times \vec{d}_{max}$ is the surface normal.

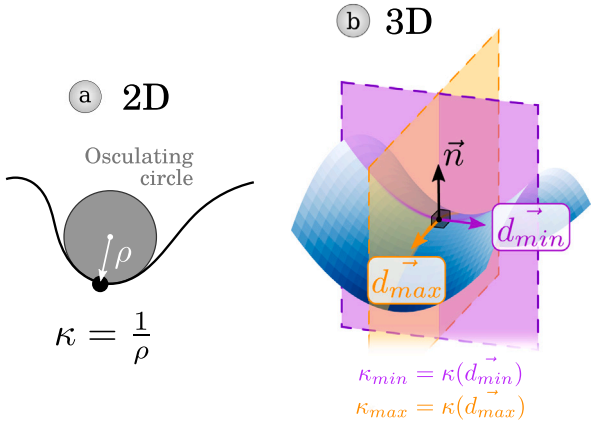

Fig. 7. (a) Definition of the curvature κ and the radius of curvature ρ for a curve in 2D. (b) Schematic representation of a saddle-like surface. The normal $\vec{n}$ and the principal directions are indicated at the saddle point. In this particular case, $\kappa_{min} < 0$ and $\kappa_{max} > 0$.

Although exact curvatures may be derived for parametric surfaces defined by analytical formulas, only estimations are possible for digital surfaces such as the one obtained by XCT. Several techniques can be used for this purpose. Integral invariants-based estimators have demonstrated their effectiveness for surfaces defined as the boundary of a collection of voxels in 3D. This method takes advantage of the fact that voxels are arranged on a regularly spaced grid, leading to interesting results in terms of both accuracy and efficiency [75]. The principle is to move a spherical convolution kernel of radius r_{curv} along the surface — see Fig. 8 for an example in 2D. Its intersection with the volume enables the estimation of some differential geometrical quantities.

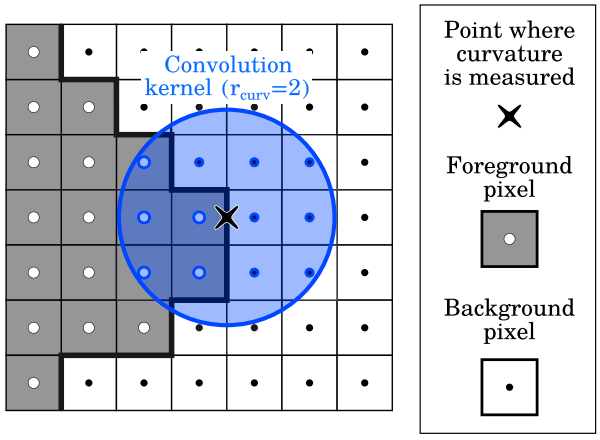

Fig. 8. Principle of integral invariant based curvature measurement from a digital shape. The example is given in 2D for clarity, but the principle remains the same for volumes. Here, the intersection area between the convolution kernel and the object is measured by counting the number of pixels whose center falls into the kernel of radius r_{curv}.

For example, κ_{mean} is directly related to the volume of the intersection between the convolution kernel and the object. Hence, an estimation of κ_{mean} at a given boundary point can be computed using Eq. (3) [76].

$$\kappa_{mean}\left(r_{curv}\right) = \frac{16}{3 \cdot r_{curv}} \cdot \left(\frac{1}{2} - \frac{V_{inter}\left(r_{curv}\right)}{\frac{4}{3} \cdot \pi \cdot r_{curv}^3}\right) \quad (3)$$

where r_{curv} is the radius of the spherical convolution kernel and $V_{inter}(r_{curv})$ is the portion of the convolution kernel's volume that resides

inside the surface's boundary. By computing the covariance matrix of the intersection instead of its volume, it is possible to design estimators for the complete curvature tensor and thus estimate likewise principal curvatures and directions [75].

Since computations are made on volumes, this offers the opportunity to perform computations using software such as ImageJ. Using Eq. (3), κ_{mean} can for instance be computed using a linear convolution. Since an optimized implementation of this method is already available in the open-source C++ library DGtal [77], it has been used in the present work.

The only parameter required to perform the calculation is the radius of the convolution kernel r_{curv}, which is the scale at which the curvature is computed. Although this parameter is of great importance and has a quite intuitive meaning, it can be difficult to properly set in practice. A first constraint that limits the possible values for r_{curv} is the resolution of the XCT scan, since a minimum of a few voxels is necessary to limit noise in the measured curvature. If one aims at minimizing the noise while keeping the curvature measurement at a fine scale, it was found useful to apply a denoising filter after curvature computation. For this purpose, we used the same Gaussian filter that was used for the S-filter in Section 3.2.

The choice of the convolution radius can also be driven by physical considerations and depends on the scale of the surface features of interest. This is the case in the example shown in Section 3.2, where curvature at a large scale can be used to detect biased roughness measurements near sharp geometrical features.

The various definitions of curvatures introduced previously are complementary because they carry different information, see e.g. Fig. 9. Depending on the objective, one definition can be more relevant than others. Mean curvature is for example a relevant parameter concerning surface tension and wetting issues [78]. Triply Periodic Minimal Surfaces (TPMS) such as gyroids, which can be manufactured using AM processes [79–82], are also characterized by a zero mean curvature. Such structures were for example found to achieve interesting energy absorption properties [83]. Gaussian curvature provides complementary information. For instance, a surface characterized by a zero Gaussian curvature is a developable surface (e.g. a cylinder). In the present work, curvature is computed with the aim to characterize surface notches and distinguish them from other surface features. The maximum and Gaussian curvatures do not seem to be suited for this purpose, as they will have the same value (zero) both on a perfectly flat surface without any notch and at the root of a linear notch in a plane.

The choice between the other curvatures being less straightforward, Fig. 9 is helpful to guide our final choice. Fig. 9b displays an artificial object showing ideal notches with different geometries. Each of those notches represents a configuration that can be found locally on a real surface, see Fig. 9a. Notches A are cups, i.e. areas where $\kappa_{min} < 0$ and $\kappa_{max} < 0$. Notch B exhibits a saddle-like geometry, with principal curvatures of opposite signs. Notches C are linear ones in a plane, i.e. $\kappa_{min} < 0$ and $\kappa_{max} = 0$. Two orientations are shown to demonstrate that it is possible to discriminate different notches based on their orientation.

Three curvatures are computed on this artificial object, namely κ_{min}, κ_{mean} and κ_{σ}. $\kappa_{\sigma} = \kappa\left(\vec{d}_{\sigma}\right)$ is the directional curvature along the direction $\vec{d}_{\sigma}$ (vertical in this case). The comparison of the three curvatures in Fig. 9c-e makes it possible to identify which one highlights best the different notches.

The first one is the minimum curvature κ_{min}, which successfully captures all notches. Furthermore, all have the same κ_{min} value. The second curvature is κ_{mean}. Cups (type A) have the lowest κ_{mean} value whereas linear notches (C) show intermediate values. This difference is not necessarily desirable, since cups are not expected to reduce the mechanical properties more than linear notches. Even worse, κ_{mean} tends to 0 for the saddle-like notch (B). Although this notch was chosen as an example for the sake of clarity and seems far from a real case, there are many regions of the surface where $\kappa_{min} < 0$ and $\kappa_{max} < 0$. Thus, κ_{mean} seems less relevant than κ_{min} to detect notches in general because it is somehow biased by the κ_{max} contribution.

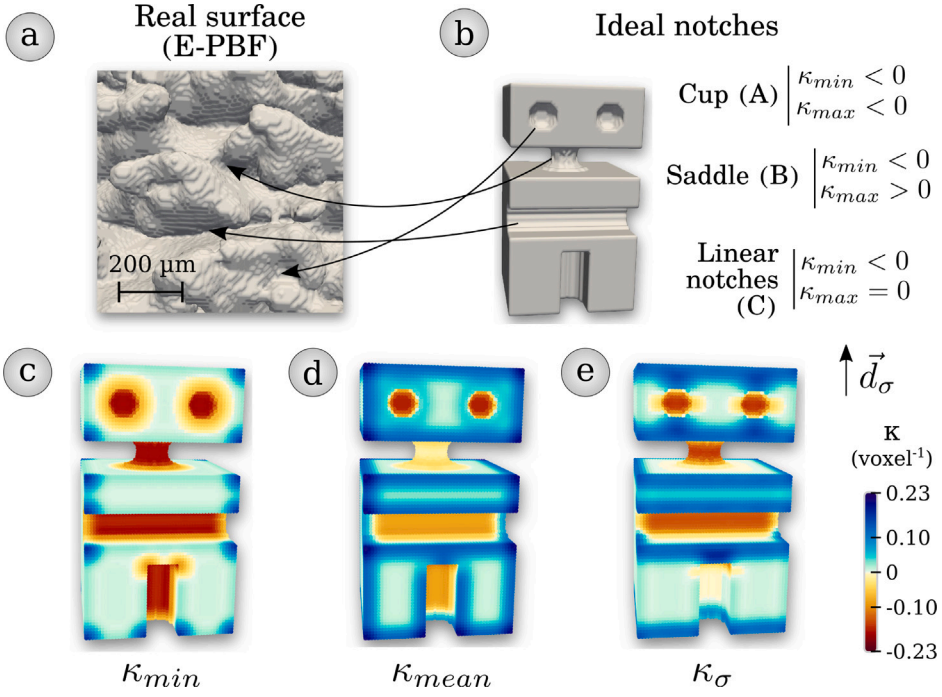

Fig. 9. Guide for the choice of relevant curvatures for the characterization of notches. (a) Notches visible on a surface mesh extracted from an XCT scan of an as-built surface inherited from E-PBF. (b) Artificial object used as model, with different types of notches. Each notch present in the artificial object shows a configuration that can be found on a real surface. (c) κ_{min}, (d) κ_{mean}, and (e) κ_{σ} measurements on the artificial object. κ_{σ} is here computed assuming that $\vec{d}_{\sigma}$ is vertical. Notch roots have by definition a radius of curvature of 5 voxels (i.e. $\kappa = 0.2$).

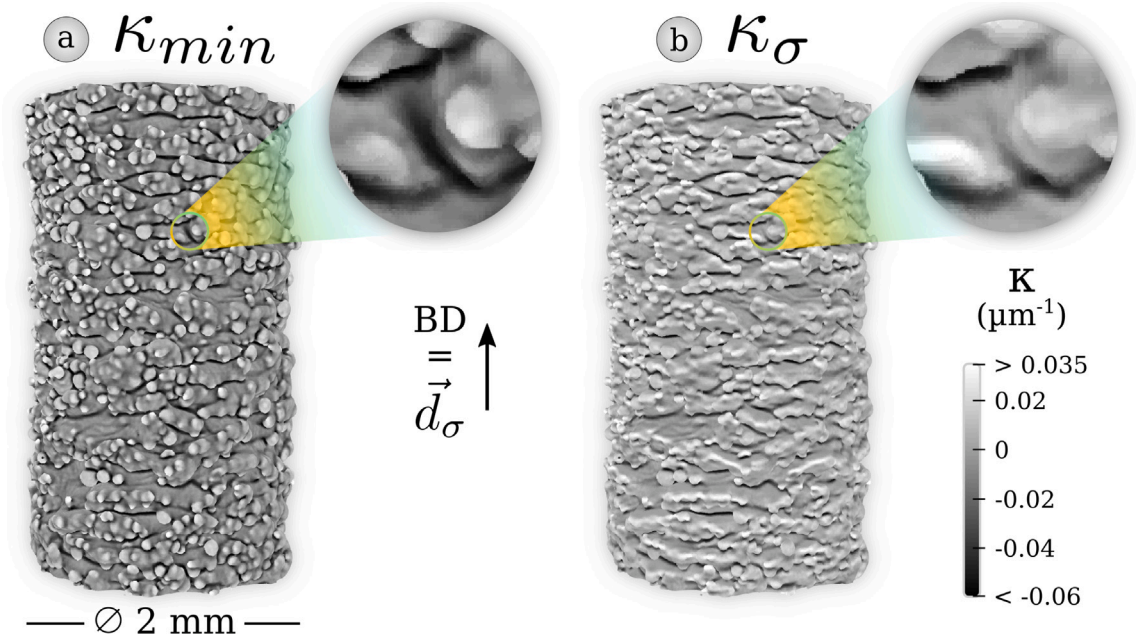

Fig. 10. (a) κ_{min} and (b) κ_{σ} measurements on an as-built cylindrical sample fabricated by E-PBF. Computations were made from an XCT scan with a voxel size of 5 µm, using r_{curv} = 30 µm = 6 voxels and λ_S = 0.025 mm = 5 voxels. The magnifying windows provide an enlarged view on a notch parallel to $\vec{d}_{\sigma}$. It shows that κ_{σ} manages to ignore it, whereas notches perpendicular to the loading direction are kept.

Finally, the third curvature is the directional one, κ_{σ}. As illustrated in Fig. 9e, all notches are well identified except the one parallel to $\vec{d}_{\sigma}$. High κ_{σ} values are also more concentrated at notches roots in comparison with κ_{min}. κ_{σ} can thus be considered the most appropriate choice when one aims at characterizing surface features with a specific orientation with respect to a loading direction.

Based on these considerations, both κ_{min} and κ_{σ} were thus computed on the same cylindrical sample used in Section 3.2, see Fig. 10a-b. Since the sample is a fatigue specimen meant to be loaded along its axis, κ_{σ} was computed along this direction. A radius of 30 µm (= 6 voxels) was chosen here for the convolution kernel. An additional filter was used similarly to what has been done for roughness, using λ_S = 0.025 mm = 5 voxels. These choices were made to provide a sufficiently detailed curvature measurement without being too much affected by noise. Fig. 10a shows that κ_{min} underlines the presence of notches, which correspond to the lowest values. κ_{σ} greatly attenuates the vertical notches, an effect that can be seen when comparing enlarged views in Figs. 10a and 10b.

3.4. Quantification of the harmfulness of surface notches

The objective here is to combine both roughness and curvature to derive a parameter accounting for the mechanical severity of surface features. For surfaces derived from AM, the surface features that are expected to have the most significant impact on mechanical properties are notches [8,84,85]. To account for this notch effect, the simple analytical formula given in Eq. (4) is used. It gives the stress concentration factor at the root of an elliptical notch in a semi-infinite panel, in the absence of plastic deformation [33]. The two parameters required to estimate the stress concentration factor K_t are the notch depth d and the radius of curvature at its root ρ (see Fig. 11). In the previous sections, d is estimated by the local height, which corresponds to roughness, while ρ was defined by the inverse of the curvature κ_{σ}.

$$K_t = 1 + 2\sqrt{\frac{d}{\rho}} \tag{4}$$

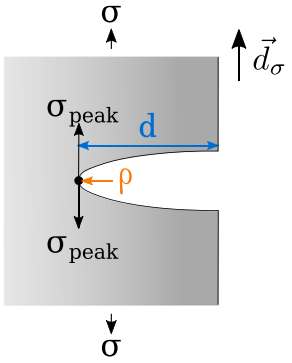

Fig. 11. Elliptical notch in a semi-infinite panel, submitted to a tensile stress σ in the direction $\vec{d}_{\sigma}$ perpendicular to the ellipse major axis. d and ρ are respectively the depth of the notch and the radius of curvature at its root. This notch generates a stress concentration given by Eq. (4), which means that the local stress at its root σ_{peak} is higher than the nominal stress in the section.

Some approximations still have to be made to apply Eq. (4) using those parameters. First, it is important to emphasize that both the roughness and curvature, as calculated in Sections 3.2 and 3.3, are estimates. Therefore, their values may depend on the method and parameters used for their measurement. The curvature values, for instance, are influenced by changes in the convolution radius r_{curv} and in the voxel size. While there are theoretical proofs, such as the one presented by Coeurjolly et al. [76], showing that integral invariant-based calculations approach exact curvature values as voxel size reduces, the resolution required to observe this might be very high. Keeping this in mind, one should treat these estimated values as semi-quantitative ones, that can for instance be used for ranking the severity of notches.

Another approximation to consider is that Eq. (4) is valid at the notch tip, which might be hard to detect automatically. As a result, the formula has been generalized and applied to every point on the surface

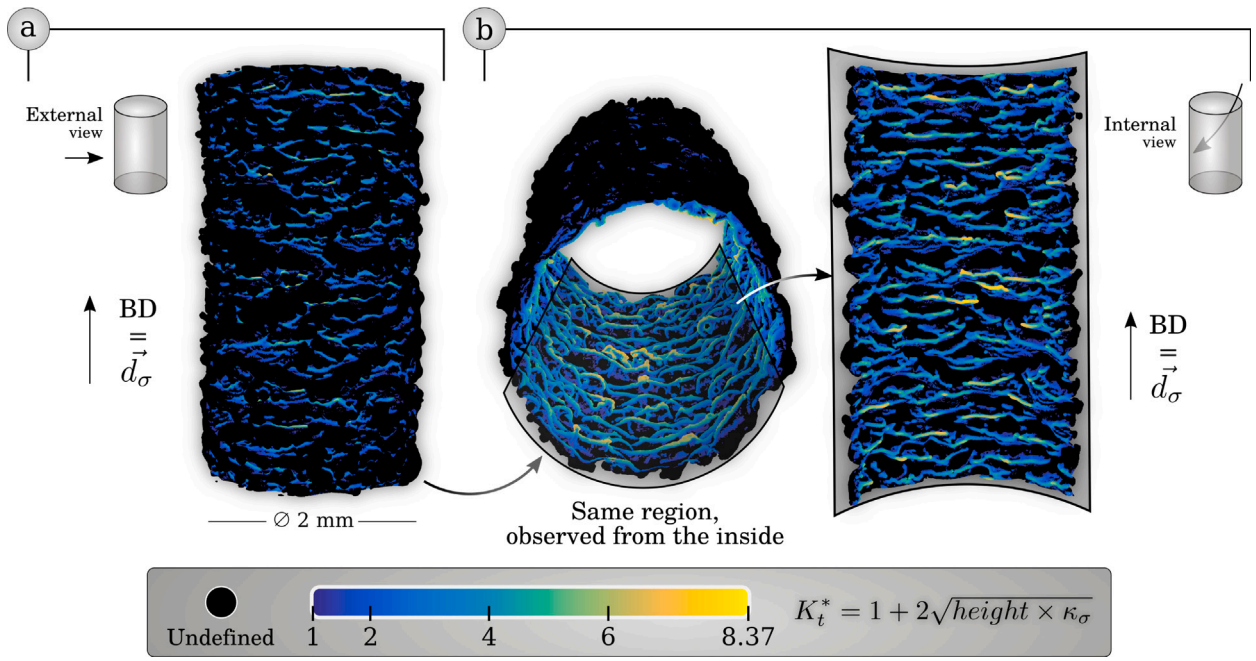

Fig. 12. K_t^* maps of a 2 mm diameter cylindrical sample fabricated by E-PBF. The K_t^* formula is given in Eq. (5) and makes use of the roughness and curvature measured in the previous sections. The curvature κ_σ is computed in the direction of the cylinder axis, which also corresponds to the build direction. The points where K_t^* is not defined — because $d \geq 0$ or $height \geq 0$ — are by default colored in black. The parameters used for computations are $\lambda_c = 0.8$ mm | $\lambda_S = 0.015$ mm for roughness, and $r_{curv} = 50$ µm | $\lambda_S = 0.025$ mm for curvature. (a) Surface as seen from the exterior of the sample. (b) Surface as seen from the interior of the sample. The internal point of view is obtained from the surface extracted from the XCT scan.

where both $\kappa_\sigma < 0$ and $d < 0$. This means it is used across the entire notches, not just at their root. While Eq. (4) might not be applicable for numerous points, the highest values will still be found at the notch roots where the depth is maximal and the curvature is minimal. Therefore, the values derived are still relevant, especially when identifying areas with the highest stress concentration. In other words, it provides a semi-quantitative parameter that reflects the mechanical severity of surface notches. Finally, an approximate value of K_t, called K_t^*, can be computed at the sample surface using Eq. (5).

$$K_t^* = 1 + 2\sqrt{height \cdot \kappa_\sigma} \text{ where } height < 0,\ \kappa_\sigma < 0 \quad (5)$$

where K_t^* is the estimated local stress concentration, $height$ is the local surface height obtained from roughness measurements and κ_σ is the directional curvature along the loading direction.

Fig. 12 shows an example of a K_t^* map computed from the same cylindrical sample used in the previous sections. Roughness and curvature (κ_σ) values used for computations are the ones presented in Sections 3.2 and 3.3.

Different views of the surface can be provided. The first one in Fig. 12a is the usual *external view*, which corresponds to what can be seen using a conventional 2.5D surface characterization. The area shown is the same as in Figs. 6 and 10. The two other views shown in Fig. 12b, are *internal views* that can be generated after extracting the surface from the XCT scan. They offer a unique way to identify deep and sharp notches that would very often be hidden using conventional characterization methods, see the comparison between Figs. 12a and 12b. Once again, this illustrates the interest in characterizing the surface as a 3D free-form one obtained by XCT.

4. Application of the developed methodology to parts with complex geometries

In order to test the ability of the methodology developed in this work to characterize complex geometries, two E-PBF Ti64 architectured materials were studied: a gyroid structure and an octet-truss lattice structure. Both would be impossible to characterize using conventional 2.5D characterization tools and methodologies.

4.1. Gyroid structure

Fig. 13a shows a picture of the studied gyroid. Two local tomography scans [86] were acquired at the center of the structure. Large artifacts were observed on the XCT scans, which made the use of the presented threshold for bimodal histograms inappropriate. Otsu's threshold was found to be more efficient in this case. To examine the influence of voxel size on roughness, curvature, and K_t^* measurements, two distinct voxel sizes were employed: 5 µm and 10 µm. In either case, roughness and curvature calculations were done using $\lambda_c = 0.8$ mm and $r_{curv} = 50$ µm.

Fig. 13b shows the measured 3D roughness map obtained from the lowest resolution scan. Two magnifying windows are also displayed to illustrate a down-skin and an up-skin region. One can clearly notice, quantitatively, the higher roughness in the down-skin area. The roughness parameters measured for both voxel sizes are summarized in Table 3. The average roughness S_a is slightly lower for the lower-resolution scan, which is consistent since a lower resolution tends to smooth the surface.

Table 3
Roughness parameters measured from the gyroid XCT scans with two voxel sizes using $\lambda_c = 0.8$ mm and $\lambda_S = 0.05$ mm. To ensure consistency between the values measured for the two voxel sizes, the parameters were evaluated using only the part of the surface available in both scans.

Voxel size (µm)	S_a (µm)	S_v (µm)	S_z (µm)	S_{sk}	S_{ku}
5	37.3	420	812	0.42	3.6
10	36.6	375	760	0.55	3.1

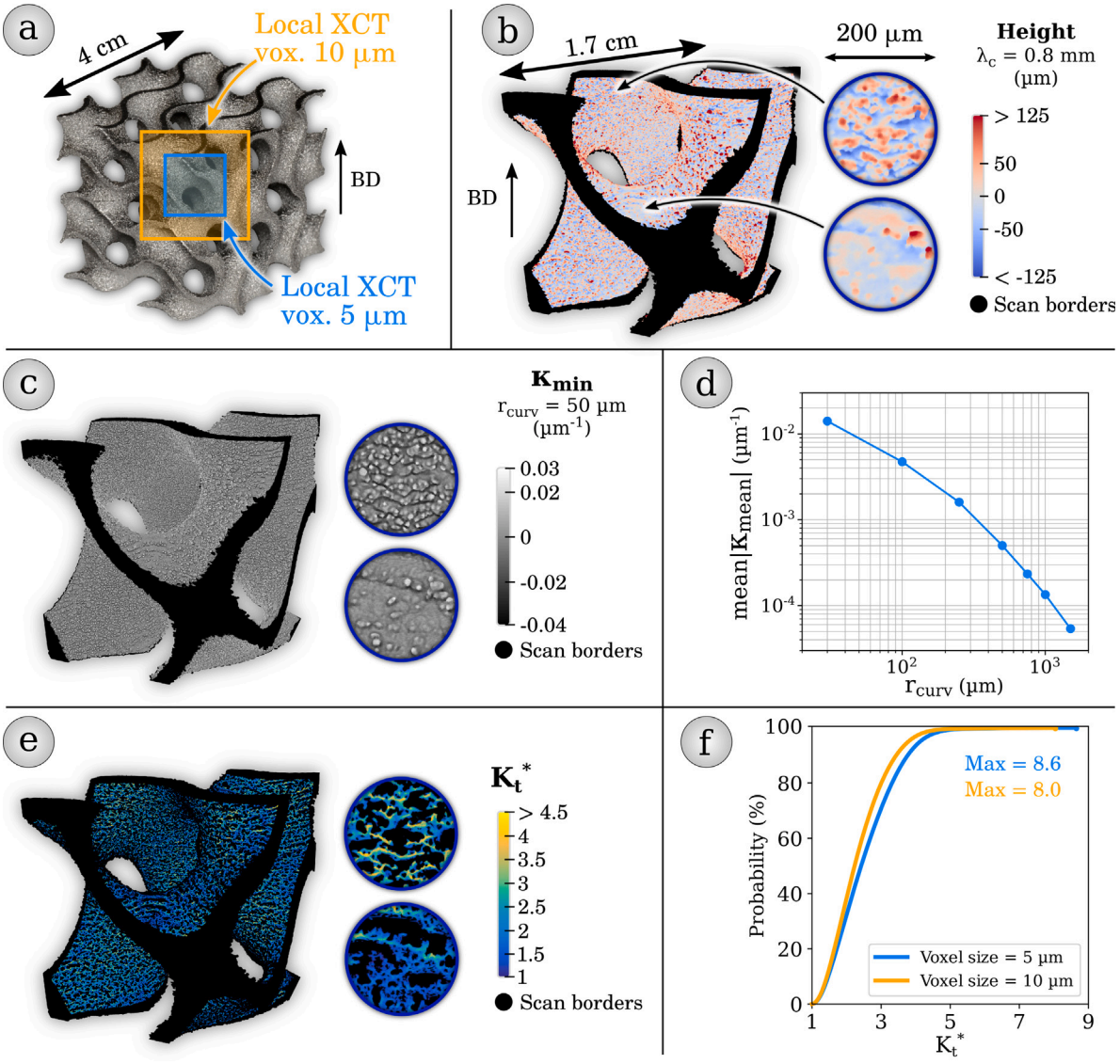

Fig. 13. 3D characterization of an E-PBF Ti64 gyroid. The 3D roughness maps shown were obtained from the XCT scan made with a 10 µm voxel size. (a) Picture of the gyroid sample. (b) 3D roughness map with magnifying windows showing a down-skin and an up-skin region (λ_c = 0.8 mm and λ_S = 0.05 mm). (c) 3D minimum curvature map with magnifying windows showing a down-skin and an up-skin region (r_{curv} = 50 µm and λ_S = 0.05 mm). (d) Cumulative distribution function of K_t^* for both voxel sizes. The same area was used for the comparison of both scans.

The higher maximum height S_z and maximum valley depth S_v are respectively 52 µm and 45 µm higher for the higher resolution scan, compared with the lower resolution one. Since the difference is roughly the same for S_z and S_v, it can be concluded in the present case that sharp and deep notches are slightly better captured using a smaller voxel size. The improvement is less significant for surface features that have positive height values such as unmelted powder particles.

The skewness S_{sk} (= asymmetry) and kurtosis S_{ku} (= sharpness) values are also consistent with this conclusion. The increase of S_{ku} with a higher resolution means that the surface height distribution contains more extreme values. The decrease in S_{sk} may also be related to the fact that notches are better taken into account. Thus, both S_{ku} and S_{sk} suggest that using a smaller voxel size allows for a better capture of notches, in particular the deepest ones.

Fig. 13c shows the 3D κ_{min} map on the same surface as Fig. 13b. Fig. 13d illustrates how curvature evolves with respect to the convolution radius r_{curv}. The mean curvature is used here since it is known that it should equal zero for an ideal gyroid, i.e. with no roughness. The average value across the entire surface is represented by the average of absolute values $mean|\kappa_{mean}|$, analogous to the role $S_a = mean|height|$ plays in roughness metrics. As observed in Fig. 13d, $mean|\kappa_{mean}|$ tends to zero with increasing r_{curv} values. This is because a larger r_{curv} measures curvature at a larger scale, corresponding more to the gyroid shape (with zero mean curvature) than microscopic surface features, which have pronounced curvatures.

Finally, Fig. 13e-f show the K_t^* measurements derived from roughness and curvature. Note that since the gyroid could be mechanically loaded in any direction, the minimum curvature is used instead of κ_σ to compute K_t^*. Fig. 13e shows the 3D K_t^* map obtained from the scan performed with a 10 µm voxel size. Meanwhile, the cumulative distribution functions of the K_t^* parameter for both voxel sizes are given in Fig. 13f. The obtained K_t^* values are slightly higher for the 5 µm voxel size scan. This can, once again, be attributed to the better ability at high resolution to properly capture sharp and deep notches.

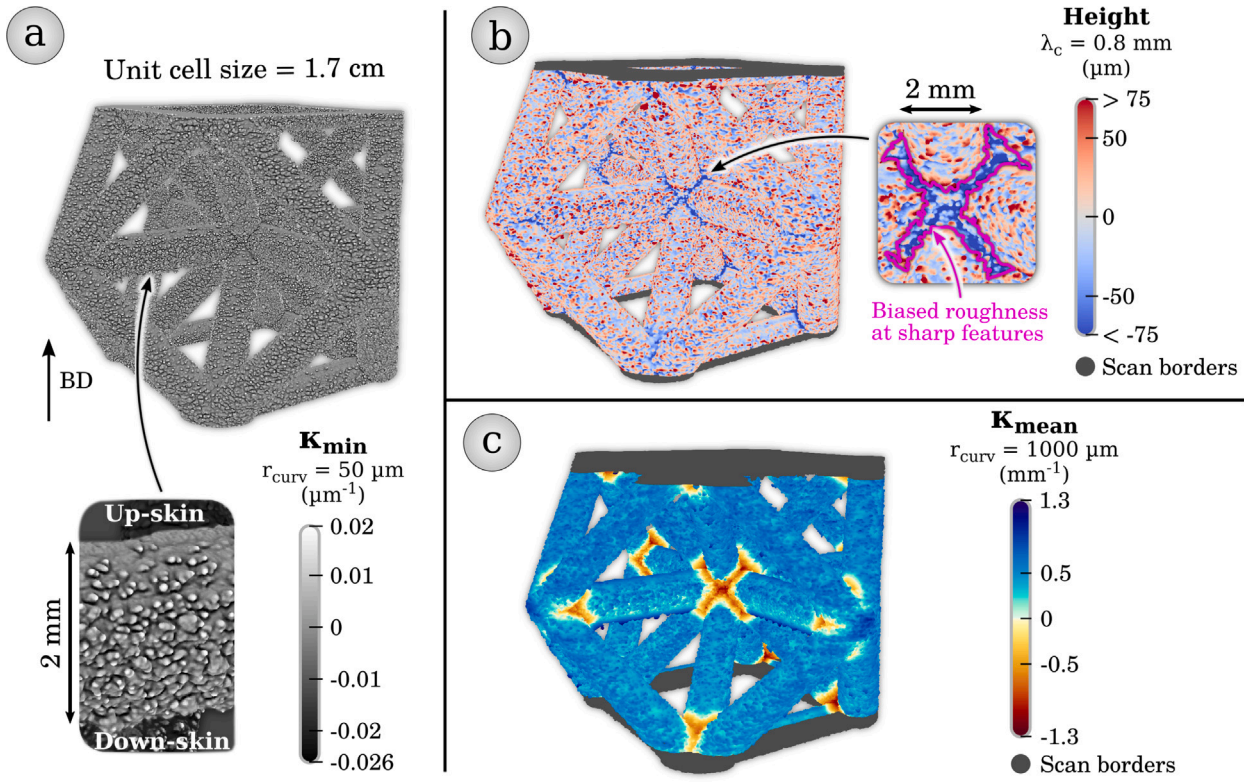

Fig. 14. 3D characterization of an E-PBF Ti64 octet-truss lattice structure. (a) 3D minimum curvature map (r_{curv} = 50 µm and λ_S = 0.05 mm). (b) 3D roughness map (λ_c = 0.8 mm and λ_S = 0.05 mm) with magnifying windows showing the region near the lattice node where roughness measurements are biased. (c) 3D mean curvature map computed at large scale (r_{curv} = 1000 µm and λ_S = 0.05 mm). Nodes, where roughness measurements are biased, are clearly identified thanks to their low mean curvature. The region highlighted in purple in b corresponds to the one with a mean curvature lower than $-0.4\,mm^{-1}$.

However, for both roughness and K_t^* measurements, the benefits from decreasing the voxel size by a factor of 2 appear rather limited. The values obtained from the two voxel sizes turn out to be in good agreement. Considering that a voxel size reduction by a factor of 2 results in an eightfold increase in volume size and limits the analysis of larger objects, the benefits might not justify the trade-offs in this case.

4.2. Octet-truss lattice structure

While the gyroid shows the ability to characterize a complex 3D structure, it is a favorable example regarding the roughness measurement. Indeed, it does not have sharp features like corners where roughness measurements will tend to be biased. To account for this effect, the second example chosen is an octet-truss lattice structure that, contrary to the gyroid case, presents sharp features. Fig. 14a shows the 3D κ_{min} map of the octet-truss. Here again, one has a good perception of the volume and surface topography details when the curvature is used for the 3D rendering.

Fig. 14b shows the 3D roughness map using a cut-off wavelength λ_c = 0.8 mm. It can be seen that roughness is successfully measured everywhere on the octet-truss lattice, except at nodes where points' height is clearly lower than it should be (see the regions delineated in purple). This shows the limit of the Gaussian filter to derive the reference surface and roughness measurements near sharp features.

It is possible to get around this issue by discarding the roughness values in those regions. This can be done manually or with the help of a mean curvature computation. In the case of the octet-truss lattice structure, the mean curvature was measured using the integral invariant approach described in Section 3.3 and a large convolution radius of 1 mm, see Fig. 14c. It can be seen that nodes are characterized by a very low mean curvature at this scale. For example, the regions delimited in purple in Fig. 14b were obtained by thresholding the mean curvature using a manually chosen value of $-0.4\,mm^{-1}$.

The limitation of this method is that it does not enable the estimation of roughness at sharp features. Those may, however, be areas of particular interest. For example, it is the case if the aim is to quantify the impact of surface roughness on mechanical properties. Indeed, sharp features will have a stress concentration effect that will add to that due to the presence of surface notches. Even though this problem is complex and has no ideal solution, more advanced smoothing methods such as anisotropic diffusion of normals [61] may be relevant in such cases as a replacement for the conventional Gaussian filter. They are indeed used to smooth surfaces while keeping sharp features of the object's form. This could lead to less biased roughness values at sharp features.

Concerning the K_t^* values obtained for complex structures, it is worth noting that the computed values estimate only the stress concentration generated by the surface topography at a micro-scale. For a more complete characterization, one may want to add the contribution of the macroscopic geometry. The latter may be computed using Finite Element Modeling (FEM) on the ideal part geometry. The same calculations could also be used to estimate locally the direction of maximum principal stress. These directions could then be used to compute the curvature instead of using a single direction for the whole part.

5. Summary

In this study, we propose a methodology for the 3D characterization of surface topography using XCT data, focusing on measuring both

roughness and 3D curvature. While this methodology has broader applications, we emphasized its usefulness on samples produced by additive manufacturing.

Key findings can be summarized as follows:

- The proposed methodology could effectively account for hidden surface features on surfaces inherited from E-PBF. For example, the 3D method can identify notches that traditional 2.5D techniques would miss.
- Our method effectively measures roughness and curvature in complex geometries such as architected structures. While the results are encouraging, some geometric features, like sharp edges, present challenges in roughness assessments. In such instances, more sophisticated metrological tools might offer deeper insights.
- We have tailored the methodology to make it accessible (see implementations in [63]), even for those unfamiliar with advanced data analysis tools and programming. For example, we deliberately used standard image analysis techniques, such as 3D Gaussian filtering, to extract roughness from the raw surface. This approach can be applied using popular software like ImageJ. With the Gaussian filter being a standard operation for the analysis of 2D and 2.5D roughness, guidelines from ISO standards can be adapted for the presented 3D workflow.
- We introduced several tools to leverage this 3D characterization in understanding the mechanical impact of surface notches. For instance, it was found that the standard Otsu's thresholding missed some of the sharpest notches. We proposed an alternative, the triangle threshold for bimodal histogram, which yielded better results in this case. Additionally, 3D curvature measurements enable the derivation of curvature in the direction of principal stress, κ_σ, underscoring the mechanical consequences of notches aligned perpendicular to the loading direction. Finally, we also proposed a model that integrates roughness and curvature data to compute a parameter, K_t^*, that reflects the stress concentration induced by surface notches.
- This method has been applied to investigate the influence of surface roughness on fatigue properties and surface crack initiation mechanisms. The study in question focuses on Ti64 samples manufactured by E-PBF and L-PBF, before and after polishing treatments. The findings are detailed in [44].

CRediT authorship contribution statement

Florian Steinhilber: Writing – original draft, Visualization, Investigation, Data curation, Conceptualization. **Joel Lachambre:** Writing – review & editing, Validation, Data curation, Conceptualization. **David Coeurjolly:** Writing – review & editing, Validation, Conceptualization. **Jean-Yves Buffiere:** Conceptualization, Supervision, Validation, Writing – review & editing. **Guilhem Martin:** Writing – review & editing, Validation, Supervision, Conceptualization. **Remy Dendievel:** Writing – review & editing, Validation, Supervision, Conceptualization.

Declaration of competing interest

The authors declare that they have no known competing financial interests or personal relationships that could have appeared to influence the work reported in this paper.

Data availability

Part of the data has been deposited on an online repository whose reference is given in the article.

Acknowledgments

This work, conducted at MATEIS and SIMaP laboratories, falls within the framework of the AEROPRINT project, which received financial support from the Auvergne-Rhône-Alpes Region and the company Dassault Aviation, France. The authors would also like to thank Théo Persenot for providing part of the data used in this paper.

Appendix. 3D Gaussian S-filter using normalized convolution

The following methodology can be used to apply any 3D linear filter on a set of voxels. In particular, it can be used to apply a Gaussian S-filter (or L-filter) to roughness values calculated following the workflow described in Section 3.2. It can be considered as a particular application case of the concept of normalized convolution introduced by Knutsson and Westin [71]. Conversely to a conventional convolution where all voxels are taken into account, normalized convolution can be used to ignore some of them. Here, it will be used to ignore background voxels and thus filter only the ones that carry actual information — i.e. the surface voxels that carry roughness values.

To go back to fundamentals, a linear filter is an operation where the value at a given voxel is replaced by a linear combination of the values at the given point and its neighbors. Each neighbor has a specific weight w, i.e. the weight of its contribution to the final filtered value. The matrix assigning the weights for the central voxel and its neighbors is called the filter kernel. For a uniform (= mean) filter, all weights are equal. In the case of a Gaussian filter, weights decrease as the distance to the central voxel increases following a Gaussian law, see Fig. A.15. In both cases, weights are generally normalized, meaning the sum of all kernel weights equals 1. For example, this ensures that applying a Gaussian filter to a uniform volume made of 1 results in a uniform volume made of 1. This is the standard "global" normalization illustrated in Fig. A.15 employed in common Gaussian filter implementations.

However, the situation is a bit different when applying a filter to a set of surface voxels. In such a case, to compute the filtered value at a given voxel, only neighbor *surface* voxels should be taken into account instead of all neighbor voxels. A solution could be to explicitly loop over surface voxels only, and never visit background voxels. This can be done in programming languages such as C++, but is completely ineffective in other languages such as Python. Thus, this approach requires some programming skills, especially to achieve reasonable computation times. Conversely, there are already many efficient implementations of the standard Gaussian filter, including ones accelerated via GPU of FFT computations. The idea here is thus to use such optimized implementations ingeniously to compute indirectly the S-filter.

To do so, the first step consists of applying a conventional Gaussian filter to the volume where surface voxels contain roughness values, while background voxels contain 0 — see step 1 in Fig. A.15. This way, background voxels do not contribute to the final filtered value. Even though, the obtained filter is not properly normalized. Indeed, the sum of the weights of all neighbors that are taken into account (i.e. all neighbor surface voxels) should equal 1. However, this sum will be in general much lower than one, because most neighbor voxels are background ones (equal to 0). To correct this bias, one simply needs to compute the same conventional Gaussian filter to a volume containing 0 at background voxels and 1 at surface voxels, see step 2 in Fig. A.15.

The resulting value at each point is the sum of all the Gaussian kernel weights that effectively come across surface voxels. It can be considered as a "local normalization factor", since by dividing the filtered value obtained in step 1 by this value, we obtain a properly normalized S-filter, see step 3 in Fig. A.15. This method is equivalent to using at each voxel a specific kernel. The latter contains 0 at background voxels, and at other voxels, a weight decreasing according to a Gaussian law with the distance to the central voxel. To be normalized, the sum of all weights must be equal to one. The trick here is to achieve such a (non-linear) computation using only linear filtration steps — i.e. using the same unique kernel for all voxels.

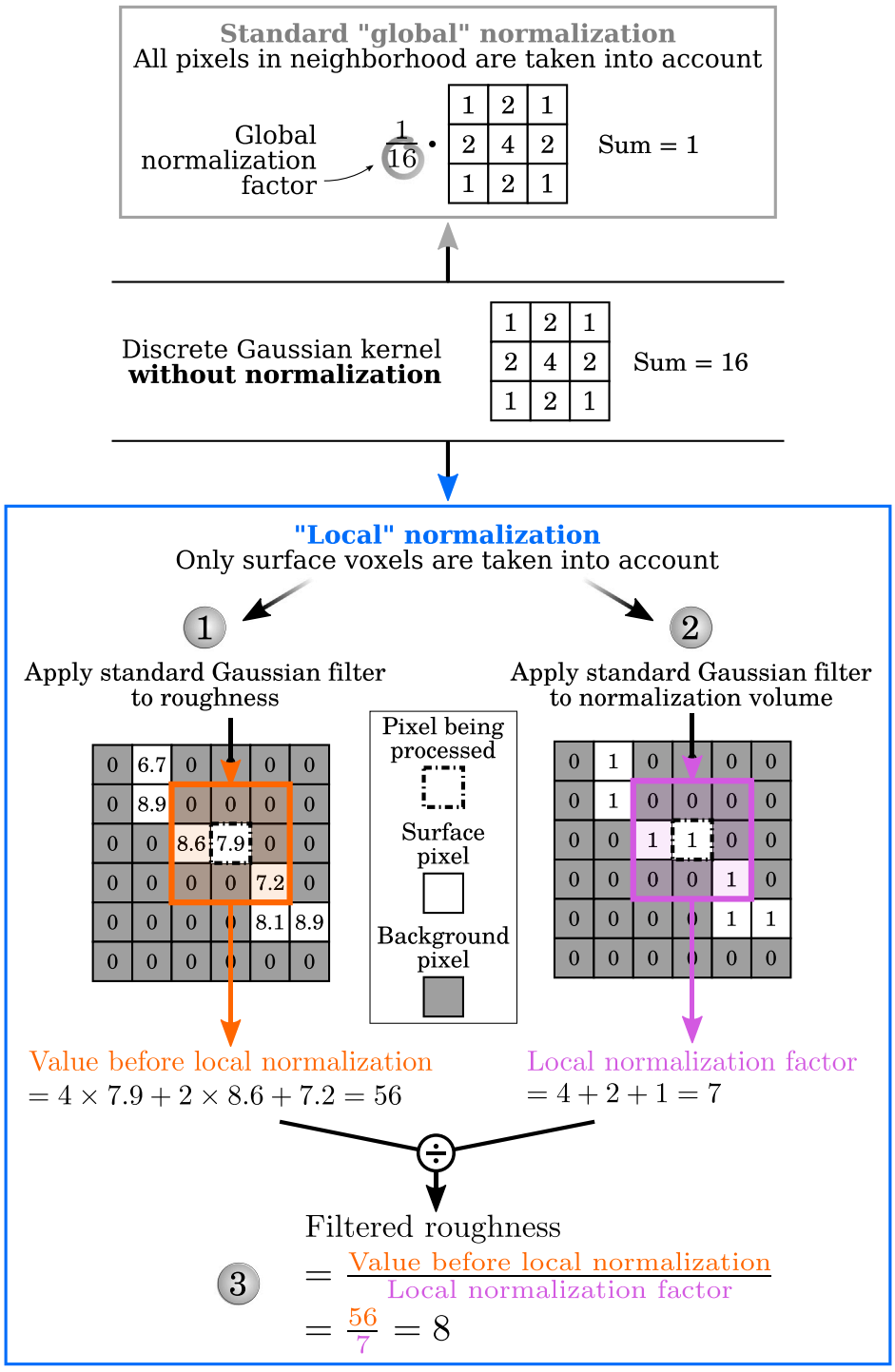

Fig. A.15. Workflow proposed for the application of a 3D Gaussian S-filter. All calculations are done using operations on digital volumes, just as the rest of the roughness computation workflow. The example provided in the present figure is restricted to 2D, which means voxels are replaced by pixels. This choice is made to facilitate understanding and visualization, considering the adaptation to a 3D case is straightforward. Note that in steps 1 and 2 of the "local normalization" in Fig. A.15, a non-normalized Gaussian filter is used for the sake of clarity only. The same steps can therefore be followed using a conventional (normalized) Gaussian filter.

References

[1] J. Dias Corpa Tardelli, A.C. Duarte Firmino, I. Ferreira, A. Cândido Dos Reis, Influence of the roughness of dental implants obtained by additive manufacturing on osteoblastic adhesion and proliferation: A systematic review, Heliyon 8 (12) (2022) http://dx.doi.org/10.1016/j.heliyon.2022.e12505, URL: https://linkinghub.elsevier.com/retrieve/pii/S2405844022037938.

[2] R.K. Alla, K. Ginjupalli, N. Upadhya, M. Shammas, R. Krishna, R. Sekhar, Surface roughness of implants: A review, Trends Biomater. Artif. Organs 25 (3) (2011) 112–118.

[3] Y.-T. Jhong, C.-Y. Chao, W.-C. Hung, J.-K. Du, Effects of various polishing techniques on the surface characteristics of the Ti-6Al-4V alloy and on bacterial adhesion, Coatings 10 (11) (2020) http://dx.doi.org/10.3390/coatings10111057, URL: https://www.mdpi.com/2079-6412/10/11/1057.

[4] K. Bohinc, G. Dražić, A. Abram, M. Jevšnik, B. Jeršek, D. Nipič, M. Kurinčič, P. Raspor, Metal surface characteristics dictate bacterial adhesion capacity, Int. J. Adhes. Adhes. 68 (2016) 39–46, http://dx.doi.org/10.1016/j.ijadhadh.2016.01.008, URL: https://linkinghub.elsevier.com/retrieve/pii/S014374961630001X.

[5] S. Sneddon, Y. Xu, M. Dixon, D. Rugg, P. Li, D.M. Mulvihill, Sensitivity of material failure to surface roughness: A study on titanium alloys Ti64 and Ti407,

Mater. Des. 200 (2021) 109438, http://dx.doi.org/10.1016/j.matdes.2020.109438, URL: https://linkinghub.elsevier.com/retrieve/pii/S0264127520309746.

[6] S. Gürgen, M.C. Kuşhan, S.F. Diltemiz, Fatigue failure in aircraft structural components, in: Handbook of Materials Failure Analysis with Case Studies from the Aerospace and Automotive Industries, Elsevier, 2016, pp. 261–277, http://dx.doi.org/10.1016/B978-0-12-800950-5.00013-2, URL: https://linkinghub.elsevier.com/retrieve/pii/B9780128009505000132.

[7] A. Toloei, V. Stoilov, D. Northwood, The relationship between surface roughness and corrosion, in: Volume 2B: Advanced Manufacturing, American Society of Mechanical Engineers, San Diego, California, USA, 2013, http://dx.doi.org/10.1115/IMECE2013-65498, URL: https://asmedigitalcollection.asme.org/IMECE/proceedings/IMECE2013/56192/San%20Diego,%20California,%20USA/260989.

[8] T. Persenot, A. Burr, G. Martin, J.-Y. Buffiere, R. Dendievel, E. Maire, Effect of build orientation on the fatigue properties of as-built electron beam melted Ti-6Al-4V alloy, Int. J. Fatigue 118 (2019) 65–76, http://dx.doi.org/10.1016/j.ijfatigue.2018.08.006.

[9] L. Deconinck, E. Bernardo Quejido, M.T. Villa Vidaller, E.A. Jägle, K. Verbeken, T. Depover, The mechanism behind the effect of building orientation and surface roughness on hydrogen embrittlement of laser powder bed fused Ti-6Al-4V, Addit. Manuf. 72 (2023) http://dx.doi.org/10.1016/j.addma.2023.103613, URL: https://linkinghub.elsevier.com/retrieve/pii/S2214860423002269.

[10] C. de Formanoir, M. Suard, R. Dendievel, G. Martin, S. Godet, Improving the mechanical efficiency of electron beam melted titanium lattice structures by chemical etching, Addit. Manuf. 11 (2016) 71–76, http://dx.doi.org/10.1016/j.addma.2016.05.001, URL: https://linkinghub.elsevier.com/retrieve/pii/S2214860416300847.

[11] N. Soro, N. Saintier, J. Merzeau, M. Veidt, M.S. Dargusch, Quasi-static and fatigue properties of graded Ti–6Al–4V lattices produced by laser powder bed fusion (LPBF), Addit. Manuf. 37 (2021) http://dx.doi.org/10.1016/j.addma.2020.101653, URL: https://linkinghub.elsevier.com/retrieve/pii/S2214860420310253.

[12] N. Sanaei, A. Fatemi, Defects in additive manufactured metals and their effect on fatigue performance: A state-of-the-art review, Prog. Mater. Sci. 117 (2021) http://dx.doi.org/10.1016/j.pmatsci.2020.100724, URL: https://linkinghub.elsevier.com/retrieve/pii/S0079642520300888.

[13] A. Charles, M. Bayat, A. Elkaseer, L. Thijs, J.H. Hattel, S. Scholz, Elucidation of dross formation in laser powder bed fusion at down-facing surfaces: Phenomenon-oriented multiphysics simulation and experimental validation, Addit. Manuf. 50 (2022) http://dx.doi.org/10.1016/j.addma.2021.102551, URL: https://linkinghub.elsevier.com/retrieve/pii/S2214860421006989.

[14] I. Mingareev, T. Bonhoff, A.F. El-Sherif, W. Meiners, I. Kelbassa, T. Biermann, M. Richardson, Femtosecond laser post-processing of metal parts produced by laser additive manufacturing, J. Laser Appl. 25 (5) (2014) 5.

[15] M. Hamidi Nasab, S. Romano, D. Gastaldi, S. Beretta, M. Vedani, Combined effect of surface anomalies and volumetric defects on fatigue assessment of AlSi7Mg fabricated via laser powder bed fusion, Addit. Manuf. 34 (2020) http://dx.doi.org/10.1016/j.addma.2019.100918, URL: https://linkinghub.elsevier.com/retrieve/pii/S2214860419310991.

[16] J.C. Fox, F. Kim, Z. Reese, C. Evans, Complementary use of optical metrology and X-ray computed tomography for surface finish and defect detection in laser powder bed fusion additive manufacturing, Am. Soc. Precis. Eng. 69 (2018) 195–200.

[17] A. Townsend, N. Senin, L. Blunt, R.K. Leach, J. Taylor, Surface texture metrology for metal additive manufacturing: A review, Precis. Eng. 46 (2016) 34–47.

[18] U. Ali, Internal surface roughness enhancement of parts made by laser powder-bed fusion additive manufacturing, Vacuum 177 (2020).

[19] H. Haitjema, Uncertainty estimation of 2.5-D roughness parameters obtained by mechanical probing, Int. J. Precis. Technol. 3 (4) (2013) 403–412, http://dx.doi.org/10.1504/IJPTECH.2013.058260, URL: http://www.inderscience.com/link.php?id=58260.

[20] A. Thompson, Surface Texture Measurement of Metal Additively Manufactured Parts by X-ray Computed Tomography (Ph.D. thesis), University of Nottingham, 2018.

[21] X.J. Jiang, P.J. Scott, Advanced Metrology: Freeform Surfaces, Academic Press, London, 2020.

[22] H.S. Abdul-Rahman, J. Jiang, P.J. Scott, A Gaussian-like filtering algorithm for freeform surfaces represented by triangular meshes, 2013, http://dx.doi.org/10.13140/RG.2.1.4443.0327, URL: http://rgdoi.net/10.13140/RG.2.1.4443.0327, Publisher: Unpublished.

[23] R. Wang, A.C. Law, D. Garcia, S. Yang, Z. Kong, Development of structured light 3D-scanner with high spatial resolution and its applications for additive manufacturing quality assurance, Int. J. Adv. Manuf. Technol. 117 (3–4) (2021) 845–862, http://dx.doi.org/10.1007/s00170-021-07780-2, URL: https://link.springer.com/10.1007/s00170-021-07780-2.

[24] M. Shahpaski, L.R. Sapaico, S. Süsstrunk, Surface roughness estimation using structured light projection, Electron. Imaging 33 (5) (2021) http://dx.doi.org/10.2352/ISSN.2470-1173.2021.5.MAAP-139, URL: https://library.imaging.org/ei/articles/33/5/art00005.

[25] A. Townsend, L. Pagani, P. Scott, L. Blunt, Areal surface texture data extraction from X-ray computed tomography reconstructions of metal additively manufactured parts, Precis. Eng. 48 (2017) 254–264, http://dx.doi.org/10.1016/j.precisioneng.2016.12.008, URL: https://linkinghub.elsevier.com/retrieve/pii/S0141635916303518, tex.ids=Townsend_2017a.

[26] S. Lou, L. Pagani, W. Zeng, M.U. Ghori, X. Jiang, P.J. Scott, Surface texture evaluation of additively manufactured metallic cellular scaffolds for acetabular implants using X-ray computed tomography, Bio-Des. Manuf. 2 (2) (2019) 55–64, http://dx.doi.org/10.1007/s42242-019-00042-x, URL: http://link.springer.com/10.1007/s42242-019-00042-x.

[27] F. Zanini, L. Pagani, E. Savio, S. Carmignato, Characterisation of additively manufactured metal surfaces by means of X-ray computed tomography and generalised surface texture parameters, CIRP Ann. 68 (1) (2019) 515–518, http://dx.doi.org/10.1016/j.cirp.2019.04.074, URL: https://linkinghub.elsevier.com/retrieve/pii/S0007850619301039.

[28] M. Grazia Guerra, F. Lavecchia, Measurement of additively manufactured freeform artefacts: The influence of surface texture on measurements carried out with optical techniques, Measurement 209 (2023) http://dx.doi.org/10.1016/j.measurement.2023.112540, URL: https://linkinghub.elsevier.com/retrieve/pii/S0263224123001045.

[29] J.W. McBride, K.J. Cross, The surface area and localised 3D roughness of a highly structured surface using X-ray Computed Tomography (XCT), Metrol. Lett. (2020).

[30] L. Pagani, S. Lou, W. Zeng, X. Jiang, P.J. Scott, Effect of the form estimation on the areal texture parameters for X-ray computed tomography measurement, in: Proc iCT 2018, 2018.

[31] G. Kerckhofs, G. Pyka, M. Moesen, J. Schrooten, M. Wevers, High-resolution micro-CT as a tool for 3D surface roughness measurement of 3D additive manufactured porous structures, in: Proc iCT, 2012.

[32] J.J. Lifton, Y. Liu, Z.J. Tan, B. Mutiargo, X.Q. Goh, A.A. Malcolm, Internal surface roughness measurement of metal additively manufactured samples via X-ray CT: the influence of surrounding material thickness, Surf. Topogr.: Metrol. Properties 9 (3) (2021) http://dx.doi.org/10.1088/2051-672X/ac0e7c, URL: https://iopscience.iop.org/article/10.1088/2051-672X/ac0e7c.

[33] C. Inglis, Stresses in plates due to the presence of cracks and sharp corners, in: Spie Milestone series MS, vol. 137, 1913, pp. 3–17.

[34] H. Neuber, Theory of Notch Stresses: Principles for Exact Calculation of Strength with Reference to Structural Form and Material, 1958.

[35] D. Arola, M. Ramulu, An examination of the effects from surface texture on the strength of fiber reinforced plastics, J. Compos. Mater. 33 (2) (1999) 102–123, http://dx.doi.org/10.1177/002199839903300201, URL: http://journals.sagepub.com/doi/10.1177/002199839903300201.

[36] S. Lee, B. Rasoolian, D.F. Silva, J.W. Pegues, N. Shamsaei, Surface roughness parameter and modeling for fatigue behavior of additive manufactured parts: A non-destructive data-driven approach, Addit. Manuf. 46 (2021) http://dx.doi.org/10.1016/j.addma.2021.102094, URL: https://linkinghub.elsevier.com/retrieve/pii/S2214860421002591.

[37] S. McKelvey, A. Fatemi, Surface finish effect on fatigue behavior of forged steel, Int. J. Fatigue 36 (1) (2012) 130–145, http://dx.doi.org/10.1016/j.ijfatigue.2011.08.008, URL: https://linkinghub.elsevier.com/retrieve/pii/S0142112311002180.

[38] A. Cellier, F. Chalon, V. Grimal-Perrigouas, D. Bonhoure, R. Leroy, Effects of cutting angles in Ti-6Al-4v milling process on surface integrity: Influence of roughness and residual stresses on fatigue limit, Mach. Sci. Technol. 18 (4) (2014) 565–584, http://dx.doi.org/10.1080/10910344.2014.955369, URL: http://www.tandfonline.com/doi/abs/10.1080/10910344.2014.955369.

[39] D. Arola, C. Williams, Estimating the fatigue stress concentration factor of machined surfaces, Int. J. Fatigue 24 (9) (2002) 923–930, http://dx.doi.org/10.1016/S0142-1123(02)00012-9, URL: https://linkinghub.elsevier.com/retrieve/pii/S0142112302000129.

[40] F. Quan, Z. Chen, H. Ye, C. Cui, Y. Cui, Study of the effect of surface roughness on fatigue strength of GH4169 based on indirect evaluation of the notch root radius, Int. J. Fatigue 152 (2021) http://dx.doi.org/10.1016/j.ijfatigue.2021.106440, URL: https://linkinghub.elsevier.com/retrieve/pii/S0142112321002991.

[41] V. Mereuta, M. Buciumeanu, L. Palaghian, 3D roughness parameters as factors in determining the evolution of effective stress concentration factors in fatigue processes, Appl. Mech. Mater. 248 (2012) 504–510, http://dx.doi.org/10.4028/www.scientific.net/AMM.248.504, URL: https://www.scientific.net/AMM.248.504.

[42] V.-D. Le, E. Pessard, F. Morel, S. Prigent, Effect of the surface roughness on the high cycle fatigue behaviour of Ti-6Al-4V alloy obtained by additive manufacturing process, Eng. Integr. 53 (2021).

[43] S. Pomberger, M. Stoschka, R. Aigner, M. Leitner, R. Ehart, Areal fatigue strength assessment of cast aluminium surface layers, Int. J. Fatigue 133 (2020) http://dx.doi.org/10.1016/j.ijfatigue.2019.105423, URL: https://linkinghub.elsevier.com/retrieve/pii/S0142112319305274.

[44] F. Steinhilber, On the use of X-ray computed tomography to investigate the influence of surface integrity on the fatigue properties of additively manufactured Ti64 (Ph.D. thesis), Université de Lyon, Lyon, 2024.

[45] T. Persenot, Fatigue of Ti-6Al-4V Thin Parts Made by Electron Beam Melting (Ph.D. thesis), Université de Lyon, Lyon, 2018.

[46] A.H. Schoen, Infinite Periodic Minimal Surfaces Without Self-Intersections, Technical Report D-5541, NASA, 1970.

[47] L. Yang, C. Yan, W. Cao, Z. Liu, B. Song, S. Wen, C. Zhang, Y. Shi, S. Yang, Compression–compression fatigue behaviour of gyroid-type triply periodic minimal surface porous structures fabricated by selective laser melting, Acta Mater. 181 (2019) 49–66, http://dx.doi.org/10.1016/j.actamat.2019.09.042, URL: https://linkinghub.elsevier.com/retrieve/pii/S1359645419306329.

[48] L.A. Feldkamp, L.C. Davis, J.W. Kress, Practical cone-beam algorithm, J. Opt. Soc. Amer. A 1 (6) (1984) http://dx.doi.org/10.1364/JOSAA.1.000612, URL: https://opg.optica.org/abstract.cfm?URI=josaa-1-6-612.

[49] P. Jain, V. Tyagi, A survey of edge-preserving image denoising methods, Inform. Syst. Front. 18 (1) (2016) 159–170, http://dx.doi.org/10.1007/s10796-014-9527-0, URL: http://link.springer.com/10.1007/s10796-014-9527-0.

[50] Y. Zhang, J. Gerbrands, Transition region determination based thresholding, Pattern Recognit. Lett. 12 (1) (1991) 13–23, http://dx.doi.org/10.1016/0167-8655(91)90023-F, URL: https://linkinghub.elsevier.com/retrieve/pii/016786559190023F.

[51] N. Otsu, A threshold selection method from gray-level histograms, IEEE Trans. Syst. Man Cybern. (1979).

[52] N. Vanderesse, P. Bocher, N. Nuño, A. Yánez, L.A. Hof, On the characterization of roughness and geometrical irregularities of additively manufactured single titanium-alloy struts, Addit. Manuf. 54 (2022) http://dx.doi.org/10.1016/j.addma.2022.102731, URL: https://linkinghub.elsevier.com/retrieve/pii/S221486042200135X.

[53] G.W. Zack, W.E. Rogers, S.A. Latt, Automatic measurement of sister chromatid exchange frequency, J. Histochem. Cytochem. 25 (7) (1977) 741–753, http://dx.doi.org/10.1177/25.7.70454, URL: http://journals.sagepub.com/doi/10.1177/25.7.70454.

[54] S. Pomberger, M. Stoschka, M. Leitner, Cast surface texture characterisation via areal roughness, Precis. Eng. 60 (2019) 465–481, http://dx.doi.org/10.1016/j.precisioneng.2019.09.007, URL: https://linkinghub.elsevier.com/retrieve/pii/S0141635919302818.

[55] International Organisation for Standardization, ISO 25178-3:2012 Geometrical Product Specifications (GPS) - surface texture: Areal - Part 3: Specification operators, 2012, Geneva.

[56] E. Savio, L. De Chiffre, R. Schmitt, Metrology of freeform shaped parts, CIRP Ann. 56 (2) (2007) 810–835, http://dx.doi.org/10.1016/j.cirp.2007.10.008, URL: https://linkinghub.elsevier.com/retrieve/pii/S0007850607001588.

[57] X. Jiang, X. Zhang, P.J. Scott, Template matching of freeform surfaces based on orthogonal distance fitting for precision metrology, Meas. Sci. Technol. 21 (4) (2010) http://dx.doi.org/10.1088/0957-0233/21/4/045101, URL: https://iopscience.iop.org/article/10.1088/0957-0233/21/4/045101.

[58] H. Villarraga-Gómez, C.M. Peitsch, A. Ramsey, S.T. Smith, The role of computed tomography in additive manufacturing, 69, 2018.

[59] S. Lou, W.-H. Zeng, X.-Q. Jiang, P.J. Scott, Robust filtration techniques in geometrical metrology and their comparison, Int. J. Autom. Comput. (2013) 1–8.

[60] X. Jiang, P. Cooper, P.J. Scott, Freeform surface filtering using the diffusion equation, Proc. R. Soc. A 467 (2127) (2011) 841–859, http://dx.doi.org/10.1098/rspa.2010.0307, URL: https://royalsocietypublishing.org/doi/10.1098/rspa.2010.0307.

[61] T. Tasdizen, R. Whitaker, P. Burchard, S. Osher, Geometric Surface Smoothing Via Anisotropic Diffusion of Normals, IEEE, Boston, MA, USA, 2002, pp. 125–132, http://dx.doi.org/10.1109/VISUAL.2002.1183766, URL: http://ieeexplore.ieee.org/document/1183766/.

[62] X.J. Jiang, P.J. Scott, Free-form surface filtering using wavelets and multiscale decomposition, in: Advanced Metrology, Elsevier, 2020, pp. 195–246, http://dx.doi.org/10.1016/B978-0-12-821815-0.00009-5, URL: https://linkinghub.elsevier.com/retrieve/pii/B9780128218150000095.

[63] F. Steinhilber, 3D roughness computation from XCT data - Data and Python & ImageJ implementations, 2023, Zenodo repository, Available at http://dx.doi.org/10.5281/zenodo.10276253.

[64] S. Lou, X. Jiang, P.J. Scott, Geometric computation theory for morphological filtering on freeform surfaces, Proc. R. Soc. A (2013) http://dx.doi.org/10.1098/rspa.2013.0150, URL: https://royalsocietypublishing.org/doi/10.1098/rspa.2013.0150.

[65] International Organisation for Standardization, ISO 16610-60:2015 Geometrical Product Specification (GPS) - Filtration - Part 60: Linear areal filters - Basic concepts, 2015, Geneva.

[66] S. Lou, X. Jiang, W. Sun, W. Zeng, L. Pagani, P. Scott, Characterisation methods for powder bed fusion processed surface topography, Precis. Eng. 57 (2019) 1–15, http://dx.doi.org/10.1016/j.precisioneng.2018.09.007, URL: https://linkinghub.elsevier.com/retrieve/pii/S0141635918300345.

[67] M. Vetterli, M. Schmid, K. Wegener, Comprehensive investigation of surface characterization for laser sintered parts, in: DDMC 2014 : Fraunhofer Direct Digital Manufacturing Conference : Proceedings, 2014, http://dx.doi.org/10.3929/ETHZ-A-010357719, URL: http://hdl.handle.net/20.500.11850/97466, Artwork Size: 6 p. Medium: Application/pdf Publisher: ETH Zurich.

[68] L. Pagani, A. Townsend, W. Zeng, S. Lou, L. Blunt, X.Q. Jiang, P.J. Scott, Towards a new definition of areal surface texture parameters on freeform surface: Re-entrant features and functional parameters, Measurement 141 (2019) 442–459, http://dx.doi.org/10.1016/j.measurement.2019.04.027, URL: https://linkinghub.elsevier.com/retrieve/pii/S026322411930329X.

[69] T. Hirata, A unified linear-time algorithm for computing distance maps, Inform. Process. Lett. 58 (3) (1996) 129–133, http://dx.doi.org/10.1016/0020-0190(96)00049-X, URL: https://linkinghub.elsevier.com/retrieve/pii/002001909600049X.

[70] C. Maurer, R. Qi, V. Raghavan, A linear time algorithm for computing exact Euclidean distance transforms of binary images in arbitrary dimensions, IEEE Trans. Pattern Anal. Mach. Intell. 25 (2) (2003) 265–270, http://dx.doi.org/10.1109/TPAMI.2003.1177156, URL: http://ieeexplore.ieee.org/document/1177156/.

[71] H. Knutsson, C.-F. Westin, Normalized and differential convolution, in: Proceedings of IEEE Conference on Computer Vision and Pattern Recognition, IEEE Comput. Soc. Press, New York, NY, USA, 1993, pp. 515–523, http://dx.doi.org/10.1109/CVPR.1993.341081, URL: http://ieeexplore.ieee.org/document/341081/.

[72] International Organisation for Standardization, ISO 16610-28:2016 Geometrical Product Specifications (GPS) — Filtration — Part 28: Profile filters: End effects, 2016, Geneva.

[73] D. Janecki, Edge effect elimination in the recursive implementation of Gaussian filters, Precis. Eng. 36 (1) (2012) 128–136, http://dx.doi.org/10.1016/j.precisioneng.2011.08.001, URL: https://linkinghub.elsevier.com/retrieve/pii/S0141635911001346.

[74] G. Taubin, Estimating the tensor of curvature of a surface from a polyhedral approximation, in: Proceedings of IEEE International Conference on Computer Vision, Cambridge, MA, USA, 1995, pp. 902–907, http://dx.doi.org/10.1109/ICCV.1995.466840, URL: http://ieeexplore.ieee.org/document/466840/.

[75] J.-O. Lachaud, D. Coeurjolly, J. Levallois, Robust and convergent curvature and normal estimators with digital integral invariants, in: L. Najman, P. Romon (Eds.), Modern Approaches To Discrete Curvature, Springer International Publishing, Cham, 2017, pp. 293–348, URL: http://link.springer.com/10.1007/978-3-319-58002-9_9.

[76] D. Coeurjolly, J.-O. Lachaud, J. Levallois, Multigrid convergent principal curvature estimators in digital geometry, Comput. Vis. Image Underst. 129 (2014) 27–41, http://dx.doi.org/10.1016/j.cviu.2014.04.013, URL: https://linkinghub.elsevier.com/retrieve/pii/S1077314214001003.

[77] DGtal Team, DGtal, 2022, URL: https://dgtal.org/.

[78] M.J. Blunt, Q. Lin, T. Akai, B. Bijeljic, A thermodynamically consistent characterization of wettability in porous media using high-resolution imaging, J. Colloid Interface Sci. 552 (2019) 59–65, http://dx.doi.org/10.1016/j.jcis.2019.05.026, URL: https://linkinghub.elsevier.com/retrieve/pii/S0021979719305648.

[79] L. Yuan, S. Ding, C. Wen, Additive manufacturing technology for porous metal implant applications and triple minimal surface structures: A review, Bioactive Mater. 4 (2019) 56–70, http://dx.doi.org/10.1016/j.bioactmat.2018.12.003, URL: https://linkinghub.elsevier.com/retrieve/pii/S2452199X18300768.

[80] M. Tilton, A. Borjali, J.C. Griffis, K.M. Varadarajan, G.P. Manogharan, Fatigue properties of Ti-6Al-4V TPMS scaffolds fabricated via laser powder bed fusion, Manuf. Lett. 37 (2023) 32–38, http://dx.doi.org/10.1016/j.mfglet.2023.06.005, URL: https://linkinghub.elsevier.com/retrieve/pii/S2213846323000317.

[81] C. Polley, W. Radlof, F. Hauschulz, C. Benz, M. Sander, H. Seitz, Morphological and mechanical characterisation of three-dimensional gyroid structures fabricated by electron beam melting for the use as a porous biomaterial, J. Mech. Behav. Biomed. Mater. 125 (2022) http://dx.doi.org/10.1016/j.jmbbm.2021.104882, URL: https://linkinghub.elsevier.com/retrieve/pii/S1751616121005166.

[82] D. Khrapov, M. Kozadayeva, K. Manabaev, A. Panin, W. Sjöström, A. Koptyug, T. Mishurova, S. Evsevleev, D. Meinel, G. Bruno, D. Cheneler, R. Surmenev, M. Surmeneva, Different approaches for manufacturing Ti-6Al-4V alloy with triply periodic minimal surface sheet-based structures by electron beam melting, Materials 14 (17) (2021) http://dx.doi.org/10.3390/ma14174912, URL: https://www.mdpi.com/1996-1944/14/17/4912.

[83] L. Zhang, S. Feih, S. Daynes, S. Chang, M.Y. Wang, J. Wei, W.F. Lu, Energy absorption characteristics of metallic triply periodic minimal surface sheet structures under compressive loading, Addit. Manuf. 23 (2018) 505–515, http://dx.doi.org/10.1016/j.addma.2018.08.007, URL: https://linkinghub.elsevier.com/retrieve/pii/S2214860418304688.

[84] C.A. Kantzos, R.W. Cunningham, V. Tari, A.D. Rollett, Characterization of metal additive manufacturing surfaces using synchrotron X-ray CT and micromechanical modeling, Comput. Mech. 61 (5) (2018) 575–580, http://dx.doi.org/10.1007/s00466-017-1531-z.

[85] A. du Plessis, E. Macdonald, Hot isostatic pressing in metal additive manufacturing_ X-ray tomography reveals details of pore closure, Addit. Manuf. 34 (2020).

[86] S.R. Stock, Recent advances in X-ray microtomography applied to materials, Int. Mater. Rev. 53 (3) (2008) 129–181, http://dx.doi.org/10.1179/174328008X277803, URL: http://www.tandfonline.com/doi/full/10.1179/174328008X277803.